

Lappeenranta-Lahti University of Technology LUT  
School of Engineering Science  
Double Degree Programme in Technical Physics

**Pogudin Grigorii**

**Characterisation of Low Gain Avalanche Detectors for the CMS  
Experiment**

Examiner: Prof. Erkki Lähderanta

Supervisor: D.Sc. (Tech.), Prof. Panja-Riina Luukka

## **ABSTRACT**

Lappeenranta-Lahti University of Technology LUT

School of Engineering Science

Double Degree Programme in Technical Physics

Pogudin Grigorii

### **Characterisation of Low Gain Avalanche Detectors for the CMS experiment**

Master's Thesis

2020

83 pages, 59 figures, 3 tables

Examiner: Prof. Erkki Lähderanta

Keywords: LGAD, UFSD, CMS, MTD

The aim of this thesis was to measure the current-voltage and capacitance-voltage characteristics of the latest batch of Ultra-Fast Silicon Detectors produced by Fondazione Bruno Kessler and evaluate the parameters of the detectors, such as the breakdown voltage, the full depletion voltage, the leakage current and the capacitance. The paper describes the principle of operation of silicon detectors, considers factors affecting the timing performance of sensors, and also highlights the critical features of UFSD. In the experimental part of the work, the I-V and C-V characteristics for two groups of UFSD samples are presented. Two groups differed in the concentration of acceptors in p-stop, the layout of p-stop, and the distance (the inter-pad gap) between the active regions of the sensor; the C-V method for calculating the doping profile within a detector is presented. The experimental study of the detectors was performed in the Detector Laboratory at the Helsinki Institute of Physics.

## ABBREVIATIONS

CERN	Conseil Européen pour la Recherche Nucléaire
LHC	Large Hadron Collider
HL-LHC	High-Luminosity Large Hadron Collider
LGAD	Low Gain Avalanche Detector
UFSD	Ultra-Fast Silicon Detector
SM	Standard Model
ATLAS	A Toroidal LHC Apparatus
CMS	Compact Muon Solenoid
ALICE	A Large Ion Collider Experiment
LHCb	The Large Hadron Collider Beauty Experiment
NIEL	Non-Ionizing Energy Loss
IEL	Ionising Energy Loss
4D	Four-dimensional
pp	Proton-proton
MIP	Minimum Ionizing Particle
MTD	Minimum Ionizing Particle Timing Detector
HGTD	High Granularity Timing Detector
BTL	Barrel Timing Layer
ETL	Endcap Timing Layer
SiPM	Silicon Photomultiplier
ASIC	Application-Specific Integrated Circuit
MPV	Most Probable Value
FD	Full Depletion
JTE	Junction Termination Extension
ENC	Equivalent Noise Charge
ENF	Excess Noise Factor
I-V	Current-voltage characteristic
C-V	Capacitance-voltage characteristic

## TABLE OF CONTENTS

1 INTRODUCTION.....	5
2 The Large Hadron Collider at CERN.....	6
2.1 The High-Luminosity phase of the LHC .....	9
2.2 4D tracking .....	12
2.3 The CMS and ATLAS Timing Upgrade.....	14
3 Silicon Detectors .....	19
3.1 Radiation interaction with matter.....	19
3.2 pn-junction .....	25
3.3 Working principle of a silicon detector.....	27
3.4 Shockley-Ramo's theorem and induced current .....	27
3.5 Characteristics of an operating detector .....	28
3.6 Radiation damage.....	36
4 Ultra-Fast Silicon Detectors .....	38
4.1 Time Resolution .....	38
4.2 The structure and working principle of an Ultra-Fast Silicon Detector .....	42
4.3 The multiplication mechanism.....	45
4.5 FBK Ultra-Fast Silicon Detectors campaign .....	48
4.6 FBK Ultra-Fast Silicon Detector performance .....	50
5 Experimental part .....	56
5.1 Measured Sensors.....	56
5.2 Measurement set-up .....	60
5.3 Results .....	64
5.4 Discussion of the results.....	71
SUMMARY .....	75
REFERENCES.....	77

## 1 INTRODUCTION

The combination of precise spatial and timing information for tracking particle paths which is referred to as 4D tracking, is considered as one of the ways to upgrade the ATLAS [4] and CMS [5] experiments to the high-luminosity phase of the LHC accelerator in 2025-2027.

In these experiments the proton-proton collisions happen every 25 ns, producing thousands of particles. Under these circumstances, conventional particle tracking methods face serious challenges; it was estimated that from 10 to 15% [14] of events will overlap in space so that they cannot be distinguished.

As a potential solution to the problem, the use of Ultra-Fast Silicon Detectors (UFSD) is considered. UFSDs are silicon Low Gain Avalanche Detectors (LGAD) tailored for time measurements which have the structure of a PIN diode with a special layer that provides signal amplification by 10-20 times. Experiments show that the time resolution of such detectors can reach 30 picoseconds.

## 2 The Large Hadron Collider at CERN

The Large Hadron Collider is the most powerful and largest particle accelerator in the world [2]. The organization operating the LHC is the European Organization for Nuclear Research, known as CERN, and it has 23 European member states. The LHC relates to CERN's accelerator complex, which is shown in Figures 1 and 2. The discovery of a long-awaited Higgs boson at the energies about 125 GeV on 4 July 2012 was the first fundamental discovery made using the LHC. The LHC is at the fore of efforts to understand the essential nature of the universe and help to find answers to the questions related to high energy physics such as: the presence of supersymmetry and extra dimensions; the nature of dark matter; the properties of the Higgs boson.

The LHC is a 26.7 km length superconducting accelerator, placed 100 m underground in the tunnel at the Franco-Swiss border near Geneva. The LHC can accelerate two beams of protons or ions. The former case is the primary operation mode of the LHC. Proton-proton ( $pp$ ) collisions in the LHC happen at the center-of-mass energy of 13 TeV, while the maximum value by design is 14 TeV [67].

The LHC accelerator is the last acceleration stage, after numerous particle accelerators, as shown in Figure 1. In the beginning, protons are generated by ionizing hydrogen gas with an electric discharge and then are pre-accelerated by linear particle accelerators and by synchrotrons. After that, the beam is split and directed into the LHC where two separate beams move in anticlockwise and clockwise directions. The beams are accelerated up to 6.5 TeV.

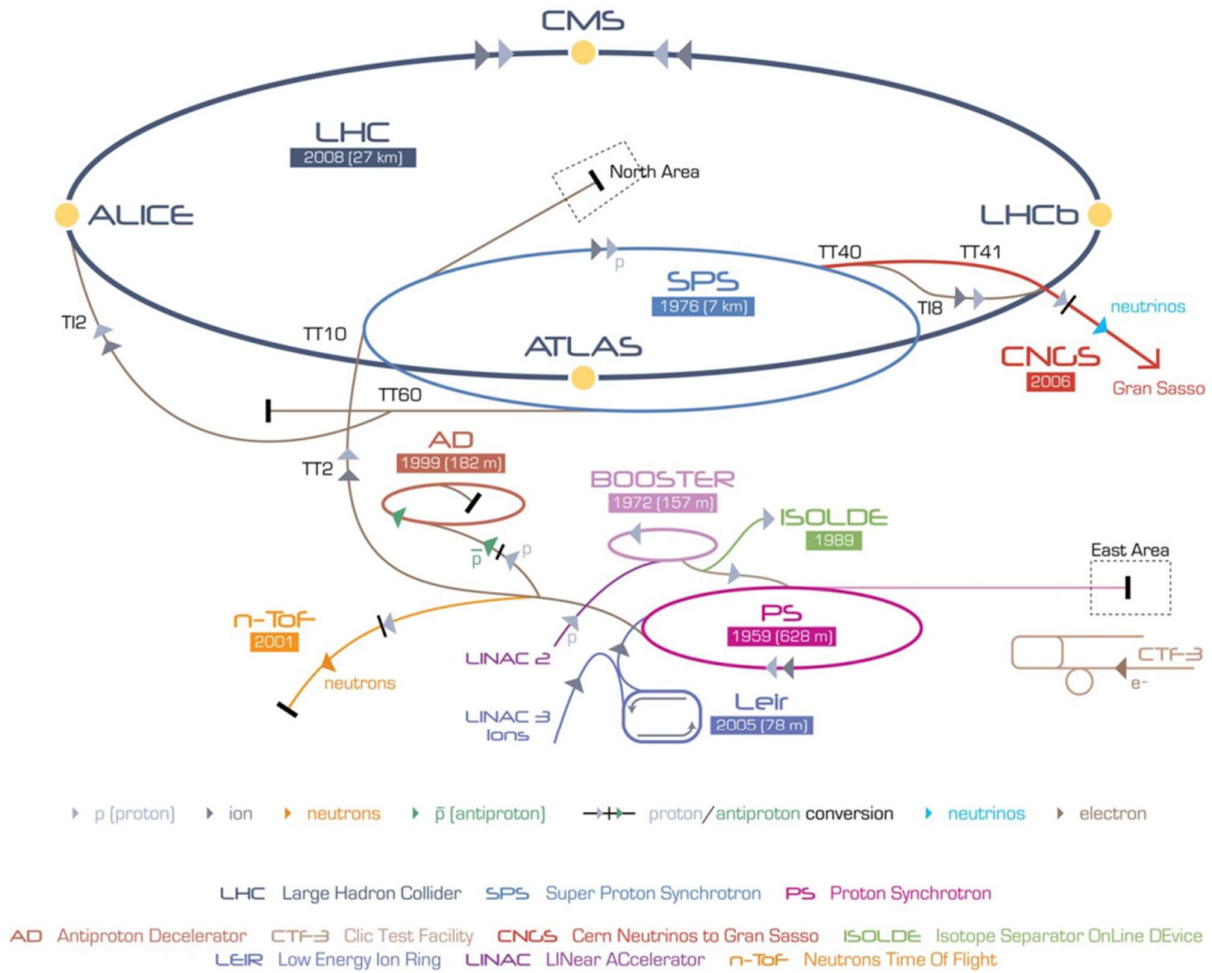


Figure 1. Scheme of the CERN accelerator complex [1]

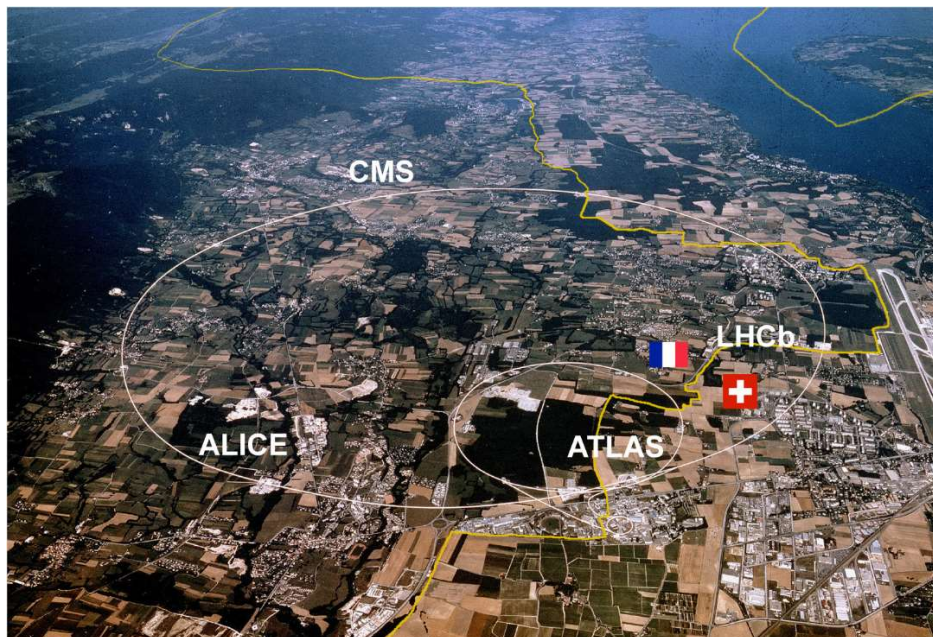


Figure 2. View of the region between the Jura mountains (left-hand side) and the Lake Geneva (right-hand side). The positions of the four experiments ATLAS, CMS, LHCb and ALICE are also shown [2]

The two beams collide in four interaction points where the main LHC experiments are installed: ALICE [3], ATLAS [4], CMS [5], LHCb [6]. These experiments are intended for various scientific programs:

- The CMS (*Compact Muon Solenoid*) and ATLAS (*A Toroidal LHC Apparatus*) experiments are so-called General Purpose Detectors (GPDs); it means that they observe any new physics phenomena that the LHC might reveal. Their physics program is focused on the investigation of the Higgs Boson properties and the search for direct signals of New Physics beyond the Standard Model.
- ALICE (*A Large Ion Collider Experiment*) in contrast to the ATLAS and CMS uses heavy ions collisions, e.g. lead ions, to study the physics of strongly interacting matter at ultimate energy densities, where quark-gluon plasma forms.
- The LHCb (*LHC beauty*) is the smallest of the four experiments. The LHCb concentrates on investigating the tenuous differences between matter and antimatter by studying a type of particle called the “beauty quark”, or “b quark”. The LHCb experiment uses a group of subdetectors to identify particles thrown forwards by the collision in one direction.

Regardless of the experiment, two groups of particles are met in the accelerator, causing many collisions, called *events*, to happen in a tiny spatial area. The number of events is characterized by a quantity called the *luminosity*. Higher luminosity enhances the chances of creating the extremely rare events that are of the most significant interest for physicists. Moreover, larger luminosity results in higher number of samples and enhanced statistical accuracy, which allows making more precise measurements. For these reasons, luminosity together with the collision energy is the most crucial performance parameter of an accelerator.

The instantaneous luminosity of a collider is a function of many accelerator design parameters [49]. It has the dimensions of events per time per area and is usually expressed in units of  $\text{cm}^{-2} \cdot \text{s}^{-1}$ . A related quantity is integrated luminosity ( $L_{\text{int}}$ ), which is the luminosity delivered to one or several particle-physics detectors over time, expressed in barns. The barn is a non-SI metric unit of area equal to  $10^{-28} \text{ m}^2$ .



Each beam in the LHC consists nominally of 2808 proton bunches spaced by 25 ns. Every bunch contains approximately one billion protons, and on average 20 protons collide at each interaction resulting in the instantaneous luminosity of  $2 \cdot 10^{34} \text{ cm}^{-2} \text{ s}^{-1}$ , achieved throughout the 2018 at CMS and ATLAS interaction points (Figure 3), that is two times higher than the LHC design luminosity ( $1 \cdot 10^{34} \text{ cm}^{-2} \text{ s}^{-1}$ ).

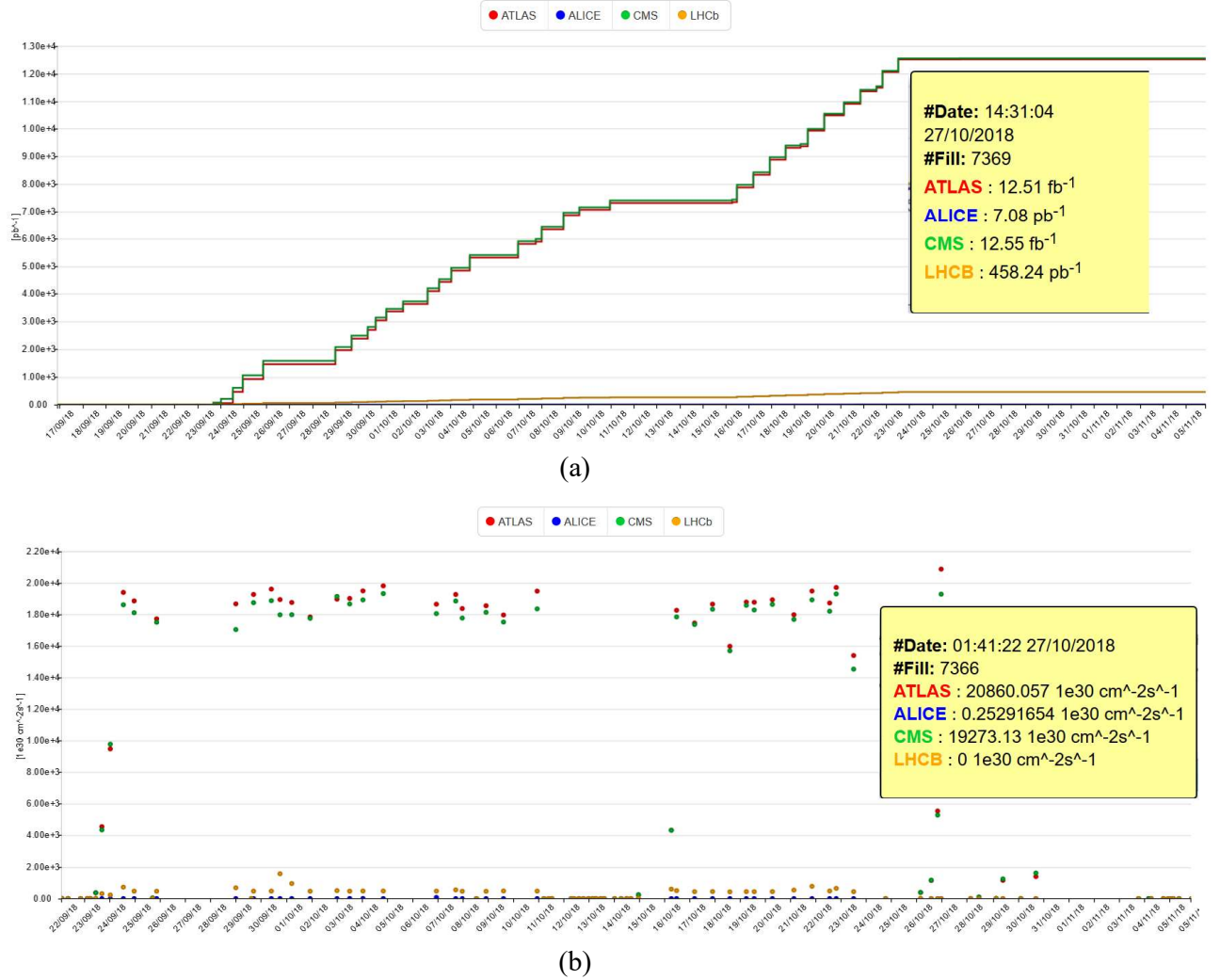


Figure 3. The integrated luminosity (a) and the peak luminosity (b) of the LHC during the second half of 2018 [7]

## 2.1 The High-Luminosity phase of the LHC

The LHC was launched in 2010 and started delivering proton-proton collisions at a centre-of-mass energy of 7 TeV in 2010-2012, and at 8 TeV from April 2012. After

that, the LHC achieved the collision energy of 13 TeV in 2015 and reached the luminosity of  $2 \cdot 10^{34} \text{ cm}^{-2}\text{s}^{-1}$  in 2018.

Throughout the Run 3 of LHC, scheduled to start in 2021, the centre-of-mass energy for proton-proton collisions is expected to be increased up to 14 TeV while the instantaneous luminosity is expected to stay at the late 2018 value, reaching a delivered integrated luminosity of  $400 \text{ fb}^{-1}$  by the end of the run. The LHC luminosity plan from 2010 to 2039 and the LHC baseline program until 2038 are shown in Figures 4 and 5, respectively.

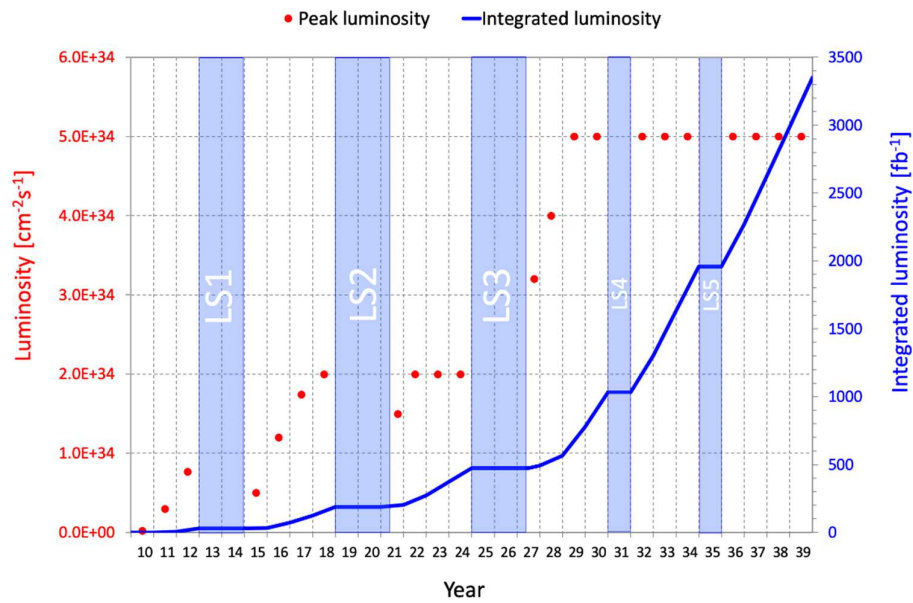


Figure 4. The LHC luminosity plan for the next two decades. Red dots indicate peak luminosity while blue line represents integrated luminosity. LS – long shutdown – main shutdown periods [8]



Figure 5. The LHC baseline plan for the next decades. The red upper line shows collision energy [8]

By around 2025-27 the LHC will be upgraded to the High-Luminosity LHC. The main objectives of the High Luminosity LHC project are to define a set of beam parameters and to build the necessary accelerator components to facilitate the LHC to reach the

target of  $5 \cdot 10^{34} \text{ cm}^{-2} \text{ s}^{-1}$  peak luminosity which results in a 10-fold increase of the LHC annual integrated luminosity; the average pile-up of 140 simultaneous proton-proton collisions occurring at each crossing of the two beams every 25 ns, with maximum values extending up to 200 interaction events per bunch crossing in the LHC detectors. To sustain the high pile-up and to entirely employ the potential of the LHC, a significant upgrade of all systems (Figure 6) has been approved.

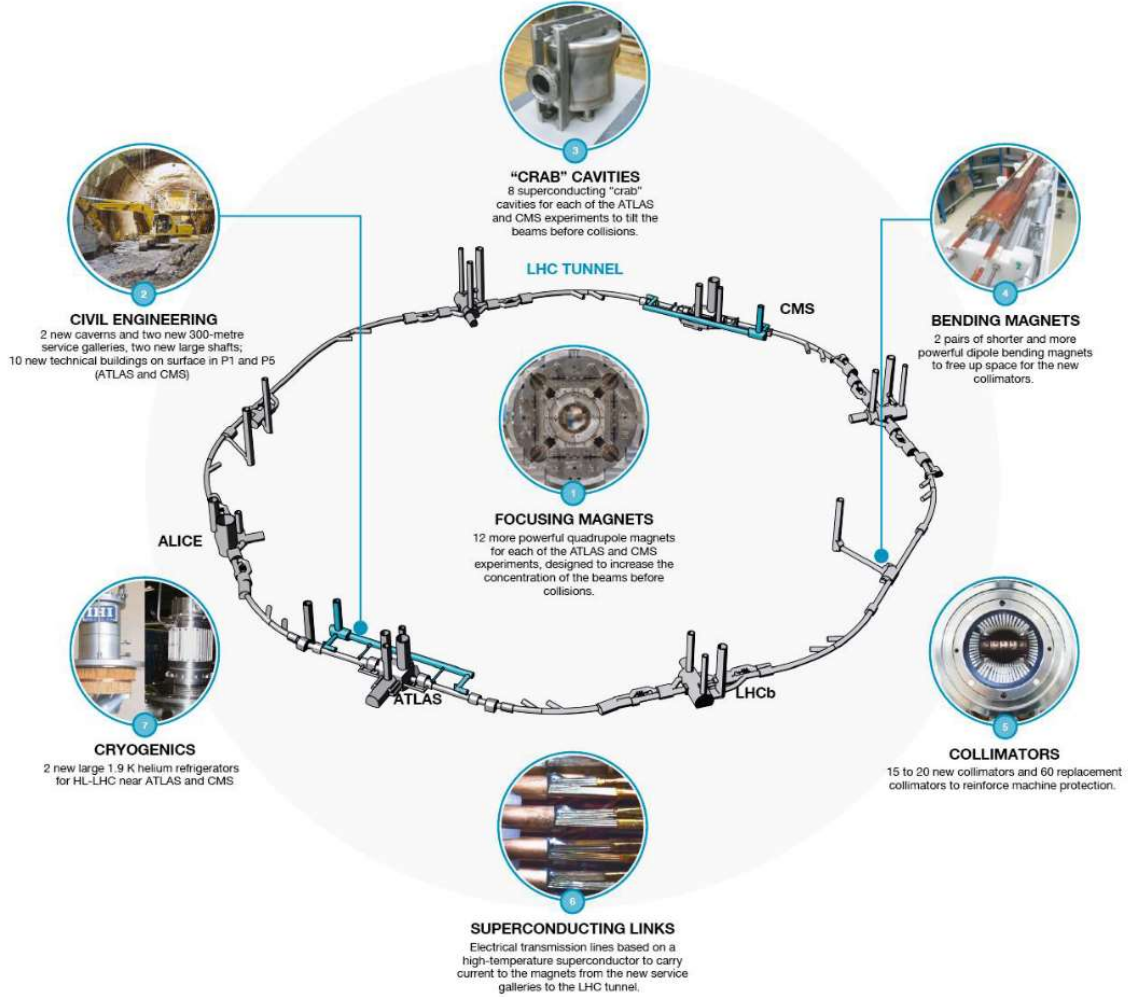


Figure 6. The overview of LHC systems to be upgraded [50]

In particular, the ATLAS and CMS experiments will experience substantial upgrades to be able to handle the increased luminosity of the HL-LHC and the harsher environment arising from the larger event pile-up, which requires highly granular, very radiation-hard silicon tracking devices in the regions closer to the beamline.

## 2.2 4D tracking

To track the events in the LHC experiments silicon detectors are widely used. In the last decades, they have proven to be an outstanding choice in large scale (more than 10 million channels) sensors, considering the fabrication process stability, the high spatial resolution, the cost, and the radiation tolerance. However, the resolution and high granularity of standard silicon detectors based on pn-junctions will not meet the time resolution requirements at the HL-LHC.

In the case of the CMS and ATLAS experiments at the HL-LHC from 140 to 200 pairs of protons will collide, generating thousands of particles (Figure 7). Due to the high pile-up conventional particle tracking techniques face drastic challenges. It has been estimated that from 10 to 15% [14] of the vertexes (the points where particles collide and interact) recognized by the tracking sensors as one vertex are in fact formed by two vertexes overlapping in space so densely that cannot be distinguished from each other. The compound of accurate time and space data in particle tracking, referred to as 4D tracking, with time resolutions of at least 30 ps would be sufficient to decrease by a factor of 5 the number of pile-up tracks per primary vertex [15].

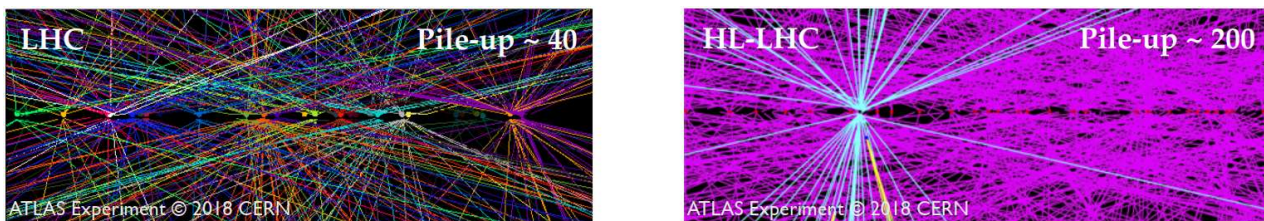


Figure 7. 40 and 200 pile-up events reconstructed in a single bunch crossing at the CERN experiment ATLAS [51]

Timing data can be obtained at several stages in the reconstruction of an event: at tracking reconstruction, if the timing information is added to each point of a track, or throughout the event reconstruction, if timing is associated to each track.

In the first case, precise time-tagging of the hits allows for the suppression of noise hits, as they would not be compatible with the expected time of passage of the particles (see Figure 8). Both the time (4D) and position (3D) measurements are included in the low-level trigger of the experiment and used directly in the real-time track-

reconstruction algorithm implemented in the processing electronics. Developing such a tracking system is a major challenge, not only for the detectors but also for the read-out electronics.

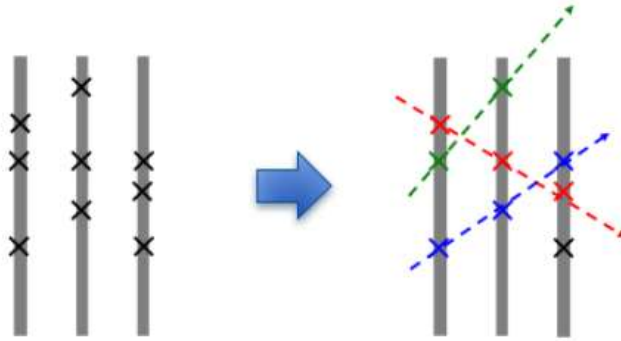


Figure 8. Including precise timing information enables the reconstruction of tracks (on the left) by associating time-compatible hits (on the right) [52]

The second method aids to reduce the burden on the electronics by time-tagging tracks rather than individual hits. It is more manageable as it demands the implementation of a separate timing layer, either outside or inside the main silicon tracker volume, to refer the timing data to every track crossing the tracker without altering the large part of the tracker hardware [18]. Figure 9 shows schematically how two overlapping events are disentangled by the help of the timing information. The transverse and longitudinal representations of tracks arising from the same vertex are presented on the left side of the picture. Due to the timing layer, the tracks can be separated into two events as shown on the right side of the figure.



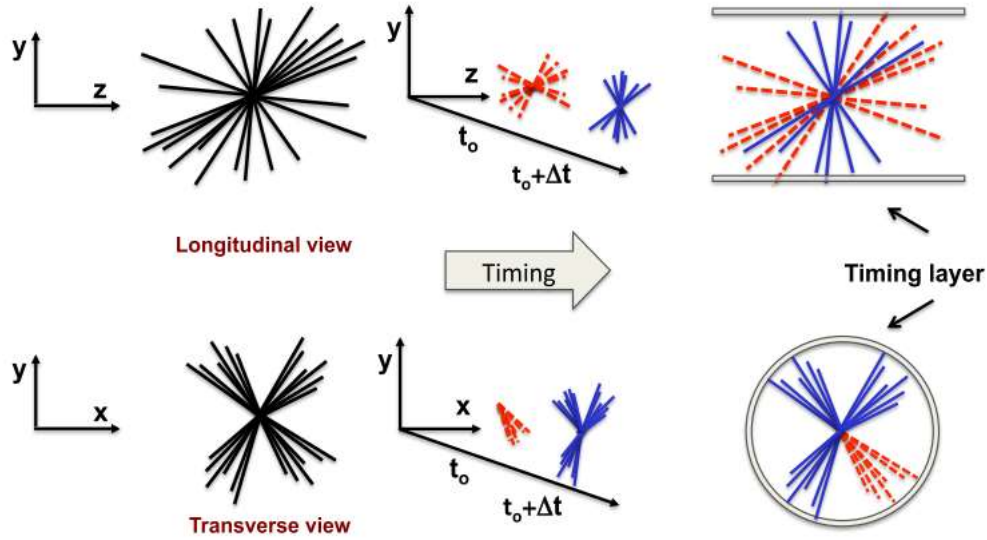


Figure 9. Schematic representation of the of the timing potential in distinguishing overlapping events utilising a separate timing layer [18]

The main component of the timing layers is timing detectors - extremely specialized sensors, which will accurately measure the *time of flight* of a particle between the production and the decay vertexes [15] assisting the tracker devices in the accurate reconstruction of each event.

### 2.3 The CMS and ATLAS Timing Upgrade

The CMS and ATLAS collaborations have embraced the method of adding timing information to each track, and not to each hit. Within this underlying common detector principle, the suggested designs of the timing layers for the CMS and ATLAS upgrades have specific differences.

#### CMS Timing Upgrade

The CMS collaboration intends to add a separate timing layer that tracks particles, with a 30-40 ps time resolution, referred to as the MIP<sup>1</sup> Timing Detector (MTD) [13, 16].

The MTD is designed as a nearly hermetic detector with coverage for a pseudorapidity range of  $|\eta| < 3$ . It is divided in a barrel region, or barrel timing layer (BTL), as illustrated in Figure 10, with coverage  $|\eta| < 1.5$  and overall detector area surface 38

<sup>1</sup> MIP - Minimum Ionizing Particle - the origin of this term will be described later

$\text{m}^2$ , and two endcaps, or endcap timing layers (ETL), which will cover  $1.6 < |\eta| < 3$  and have an overall detector area surface  $10 \text{ m}^2$  [13].

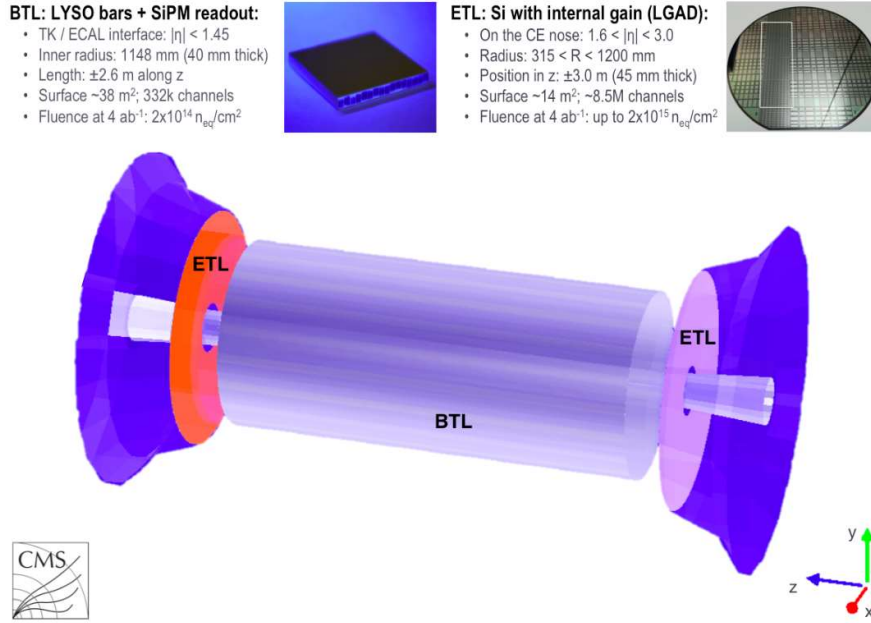


Figure 10. A schematic representation of the timing layers geometry which includes a barrel layer (grey cylinder), at the interface between the ECAL and the tracker, and two silicon endcap (orange and light violet discs) timing layers in front of the endcap calorimeter [53]

The constraints on the ETL, and BTL design and properties vary considerably. First, since radiation levels in the inner rings of the endcaps, closer to the beam pipe, will be up to a neutron-equivalent fluence of  $1.5 \cdot 10^{15} \text{ 1MeV/cm}^{-2}$ <sup>2</sup> which is a factor 30 higher than in the barrel region, different technologies have to be exploited to build these two detector regions. Then, the distinction between the density of tracks in the barrel and endcap regions leads to different sizes of the timing layer active elements to maintain their occupancy below a few per cent. This requirement ensures that useful timing information is available for as many tracks as possible and provides a large probability for single hits, needed for unequivocal time assignment. Additional constraints come from the need for integration of the timing layer within the limited space of the existing CMS detector, cost, and power budgets. All of this has led to the

<sup>2</sup>The damage happening to the device is commonly normalised to a 1 MeV equivalent neutron fluence that would result in the deposition of the same nonionising energy resulting in equivalent damage to the material. Calculation of this 1 MeV equivalent neutron damage fluence requires precise knowledge of the energy spectrum of the damaging particles [54]

choice of LYSO:Ce scintillating crystal bars readout with silicon photomultipliers (SiPMs) for the barrel and Ultra-Fast Silicon Detectors (UFSDs) for the endcaps which in this case are Low Gain Avalanche Detectors (LGADs) tailored for the timing measurements.

UFSDs are silicon detectors with an intrinsic gain of 10-30 provided by a special implant, as will be shown later, designed to overcome capacitance and other noise sources, providing a low-jitter fast-rising pulse that enables precision timing reconstruction for MIPs [20, 21]. The endcap timing layer will be set up with a two-disc system of UFSDs as active elements illustrated in Figure 11. The outer radius and inner radius of each endcap are 1200 mm and 315 mm, respectively, while its total thickness is about 45 mm. A sensor cell-size of  $2\text{ mm}^2$  at  $|\eta| \sim 3$  is required for the ETL. The choice of the detector size is a compromise between occupancy, sensor characteristics, including electronics considerations such as input capacitance and manufacturing issues, total power needs (number of channels), and cost [22, 23].

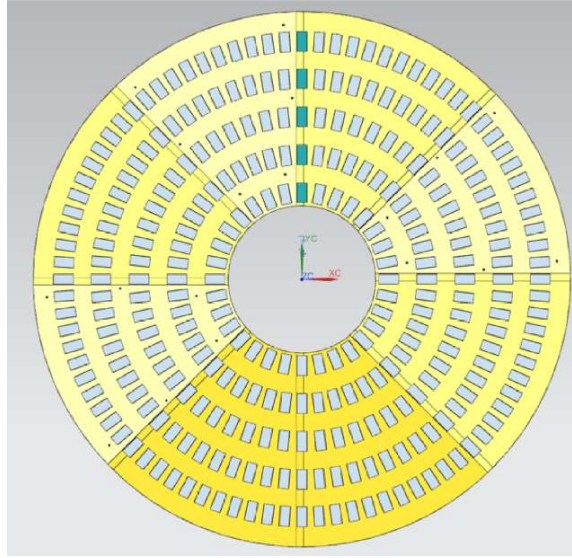


Figure 11. Overlapping disk structure with single UFSD layer provides 95% coverage, limited by the dead area between pixels [19]

The accurate time measurement provided by the MTD will bring additional time-of-flight capabilities to CMS, enhancing its performance in reconstructing physics objects under the high pile-up conditions characteristic of the HL-LHC operation. This extra



handle in mitigating pile-up effects yields significant improvements to many physics analyses by increasing signal efficiencies and improving background rejection.

### ATLAS Timing Upgrade

The *High Granularity Timing Detector* (HGTD) will enhance the performance of the ATLAS detector in the forward region and provide a robust instrument for the luminosity measurement [10]. The HGTD is going to be built in front of the endcap calorimeters cryostats of the ATLAS, at a distance  $\pm 3.5$  m from the  $pp$  collision point as shown in Figure 12 and will cover the pseudorapidity region from 2.4 to 4. As in the case for the MTD, the room to build the HGTD is limited, its inner and outer radii are 120 mm and 640 mm respectively while its entire thickness should be less than 125 mm.

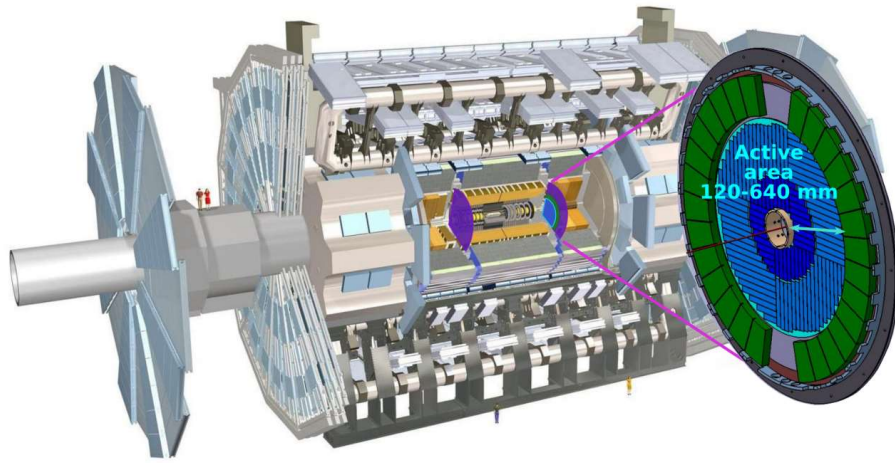


Figure 12. ATLAS HGTD placement. It will provide timing measurements for charged particles in  $2.4 < \eta < 4.0$  [24]

To guarantee a timing resolution of 30 ps per track, two layers of sensors will be coupled with read-out electronics (ASICs) to form the modules on both sides of each layer. The overlap between the back and front modules within each layer is 80% for  $R < 320$  mm and 20% for  $R > 320$  mm, as illustrated in Figure 13. The larger overlap at low radius will boost the amount of hits assigned to each track, consequently creating an additional effective layer, and thus enhancing the timing resolution in this area [24].

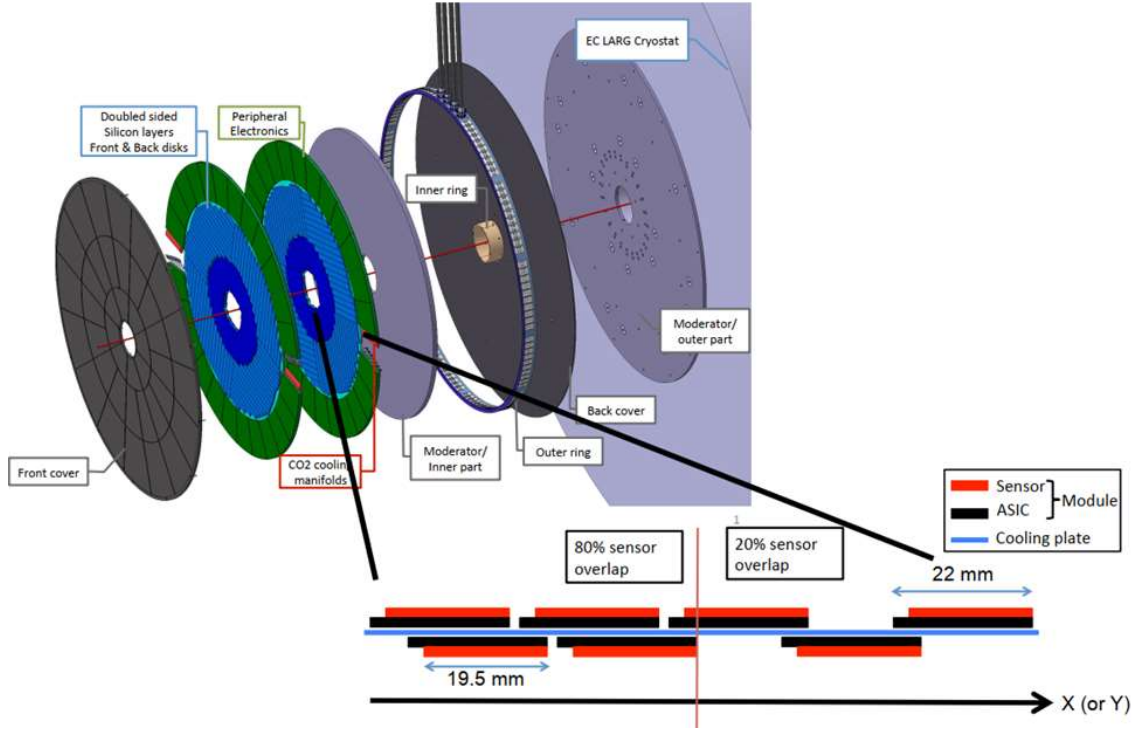


Figure 13. The proposed ATLAS High Granularity Timing Detector layout. Adapted from [24]

Owing to the huge particle rate in the HGTD area, the HGTD must be radiation hard. At the end of the HL-LHC, the maximum neutron-equivalent fluence at a radius of 120 mm will reach  $9 \cdot 10^{15} \text{ 1MeV/cm}^2$ . To withstand the high radiation level in this area, achieve the required timing resolution, and cope with the spatial limitations, sensors based on silicon were chosen, particularly UFSD sensors with a  $50 \mu\text{m}$  active thickness.

The accurate timing measurement provided by HGTD can be used to significantly advance the reconstruction of various physics objects, including the identification of b-jets and high rejection of light-quark jets, and the identification of the leptons in the forward region [24].

To sum up, for both the ATLAS and CMS upgrades the UFSDs are considered as suitable candidates to implement the 4D tracking with the help of the HGTD and the MTD. The design of UFSD sensors constantly changes, principally due to the requests of the ATLAS and CMS collaborations for the construction of their timing layers. To date to upgrade the ATLAS roughly 7000 sensors of  $2 \cdot 4 \text{ cm}^2$  are needed, each sensor with  $450 \cdot 1.3 \cdot 1.3 \text{ mm}^2$  individual pixels while the CMS requests approximately 3000

sensors of  $4.8 \cdot 9.6 \text{ cm}^2$ , each sensor with 1536  $1 \cdot 3 \text{ mm}^2$  pixels [15]. The sketches of the ATLAS and CMS modules with sensors are shown in Figure 14.

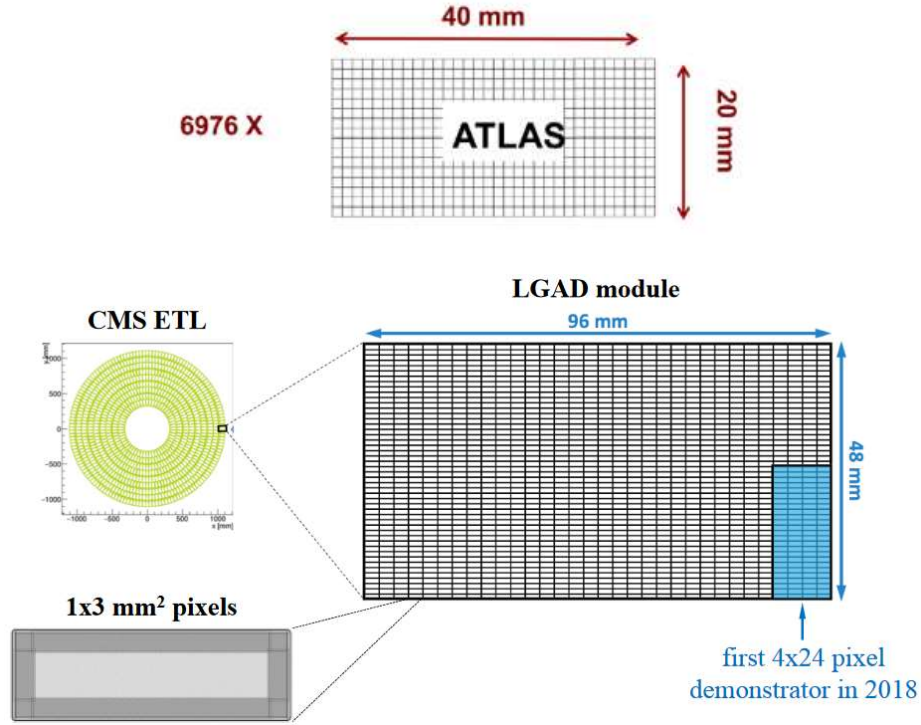


Figure 14. The proposed design of the CMS and ATLAS UFSD sensors and timing layers [15, 56]

### 3 Silicon Detectors

Silicon is the most extensively used semiconductor since it is an abundant element on Earth; technological process to grow silicon in large crystals of very high purity is relatively cheap and well-established, and it is possible to alter the electrical properties by adding specific impurity atoms - all of that makes silicon suitable in many physics applications. From the 1960s silicon has been used as a material for particle detectors in fixed-target experiments, then in the late 1980s silicon detectors have been extensively used in collider experiments as silicon pixel or silicon microstrip detectors around the initial interaction point [56].

#### 3.1 Radiation interaction with matter

The functioning of the radiation sensor relies on the manner the radiation to be detected interacts with the material of the sensor. A perception of the response of a

particular type of sensor, hence, must be based on a comprehension of the underlying mechanisms by which specific type of radiation loses energy in matter and interacts with it. There are four major categories of radiation [26]:

- a) Fast electrons
- b) Heavy charged particles (e.g. alpha particles, protons)
- c) Neutrons
- d) X-rays and gamma rays

First two categories represent the charged particle radiation that constantly interacts via the *Coulomb force* with the electrons exist in each medium that the radiation passes. Other two categories represent uncharged radiation and hence are not subjected to the Coulomb force. It means that these types of radiation need, at first, to undergo an interaction resulting in the partial or full transfer of the energy of the incident radiation to nuclei or electrons of the atoms within the medium or charged particle products of nuclear reactions. However, in some cases, the interaction does not occur within the detector, and this type of radiation (e.g., gamma rays or neutrons) may pass entirely through the detector volume without any disturbances to the medium.

The types of radiation also differ in the characteristic distance of penetration (also the *penetration depth*) or average mean free path in solids, which are  $\sim 10^{-5} \text{ m}$  for heavy charged particles,  $\sim 10^{-3} \text{ m}$  for fast electrons and  $\sim 10^{-1} \text{ m}$  for neutrons, X-rays and gamma rays. A tiny penetration depth leads to an increased possibility of signal generated closer to the surface of the material, where a signal charge can be only partly collected due to the presence of an insulation layer, doping or degeneration of the semiconductor properties. Alternatively, a huge absorption length results in a situation when radiation pass the sensor without interactions causing inefficiencies.

For any radiation type, a fraction of the energy deposited in the semiconductor is used for *ionization* process, while another part of the energy transforms into phonons, i.e. lattice vibrations, or eventually into thermal energy. Ionization is a process of creation of electron-hole pairs distributed along the length of the particle track which takes place if the energy transferred to the atom is larger than the ionization potential

of the atom. The energy of an electron-hole pair creation in semiconductors (Ge, Si) is several electronvolts.

The amount of produced electron-hole pairs is proportional to the linear stopping power  $S$  for particles in a specific material and defined as the ratio between differential energy loss for the particle inside the matter and the corresponding differential path length:

$$S = -\frac{dE}{dx}. \quad (1)$$

Relativistic charged particles except electrons lose energy in material mainly through atomic excitation and ionization processes. The mean rate of energy loss  $\frac{dE}{dx}$  is described by the Bethe-Bloch equation [27]:

$$-\frac{dE}{dx} = 4\pi \cdot m_e \cdot N_A \cdot r_e^2 \cdot z^2 \cdot c^2 \cdot \frac{Z}{A} \left[ \frac{1}{2} \cdot \ln \left( \frac{2c^2 m_e \beta^2 \gamma^2 T_{max}}{I^2} - \beta^2 - \frac{\delta(\gamma)}{2} \right) \right], \quad (2)$$

where

$T_m$  is the maximum kinetic energy that can be given to a free electron in a collision;

$E$  is the kinetic energy of the incident particle with charge  $z$ ;

$A$  and  $Z$  are the atomic mass and the atomic number of the material, respectively;

$N_A = 6.022 \cdot 10^{23} \text{ mol}^{-1}$  is the Avogadro's number;

$I$  is the mean excitation energy;

$c$  is the speed of light;

$m_e$  is the electron mass;

$\beta = v/c$  is the particle velocity;

$\gamma = \frac{1}{\sqrt{1-\beta^2}}$  the corresponding Lorentz factor;

$r_e$  is the classical electron radius;

$\delta$  is the high-energy corrective term for density.

An example of the full function of average energy loss of a traversing charged particle - a muon - is presented in Figure 15.

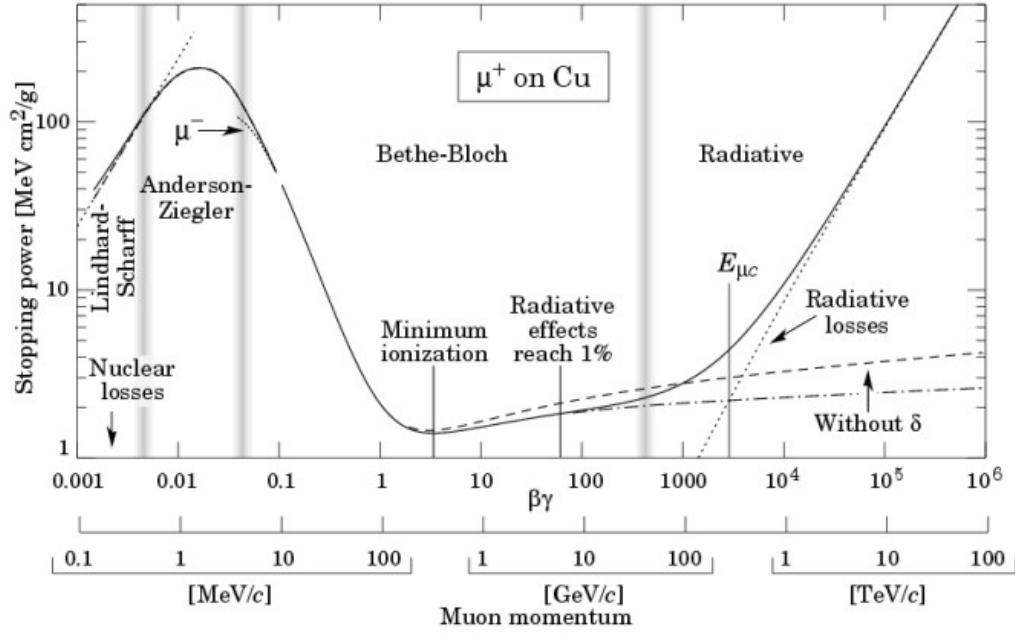


Figure 15. Energy loss of a positive muon ( $\mu^+$ ) in copper as a function of  $\beta\gamma = p/mc$  [28]

As follows from the graph, the Bethe-Bloch expression accurately characterizes the energy loss in a certain range of energies. At low energies, various corrections to the formula need to be made, whereas, at high energies, radiative effects are emerging. The energy range where the Bethe-Bloch equation is valid rely on the mass of the incident particle and the atomic number of the material [57].

A particle whose energy loss is at the minimum of the Bethe-Bloch function is referred to as the *Minimum Ionizing Particle* (MIP): this a fundamental kind of particle and each detector should have noise far less than this energy to be able to identify them. The energy loss rates of the most relativistic particles are near the MIP. Therefore, MIP can be used to calibrate detectors.

Another aspect of radiation interaction with matter is that the energy transfer per scattering, along with the amount of collisions in a finite medium, fluctuates. The energy lost by a particle in a single hit when crossing detectors follows the Landau distribution, which is an asymmetric distribution with a tail at high energies happen because of the delta rays (Figure 16). Delta rays appear when a particle loses a large amount of its energy during an interaction and the electrons produced have enough

energy to further ionize other atoms. Due to this asymmetry, the most probable value (MPV) of the distribution is 30% lower than the mean value.

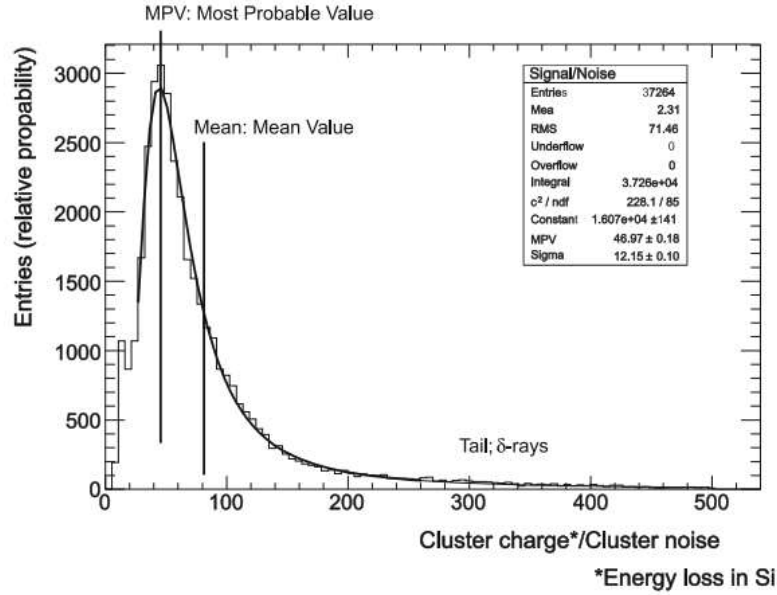


Figure 16. A Landau distribution that shows the relation between the signal charge created by MIP (cosmic particles) and noise for a 500-micrometer thick silicon [26]

In case of silicon, the energy required for one electron-hole pair to be created in the indirect semiconductor is 3.6 eV on average. For a MIP, the most probable amount of electron-hole pairs generated in one  $\mu\text{m}$  of silicon is 76, while the average is 108.

Ionization loss by positrons and electrons are different from loss by heavy particles due to the properties such as mass, spin and the way they interact with other particles.

Electrons with high energy mostly lose their energy in material due to Bremsstrahlung mechanism, while high-energy photons lose energy by production of  $e^+e^-$  pairs (Figure 17).

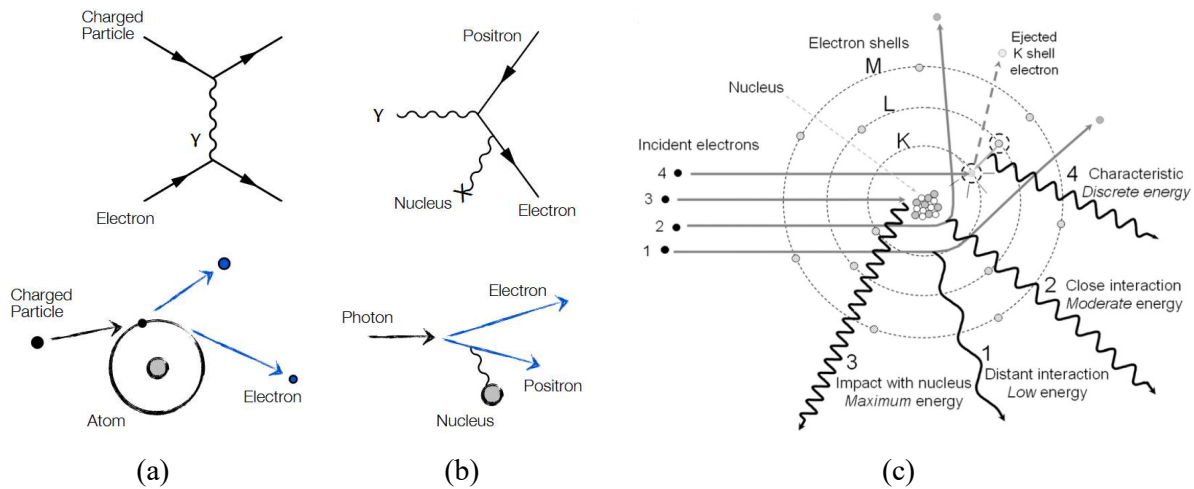


Figure 17. Examples of particle interactions: a - ionization; b - pair production; c - Bremsstrahlung (1,2,3) and characteristic radiation (4) mechanisms [58], [59]

At low energies, positrons and electrons mainly lose energy by ionization, but also processes like Bhabha scattering, Møller scattering and  $e^+$  annihilation make contribution, as depicted in Figure 18 [58]. Ionization loss rates scale up logarithmically with the energy growing, whereas losses connected with bremsstrahlung mechanism increase almost linearly and prevail for energies above a several tens of MeV in most materials.

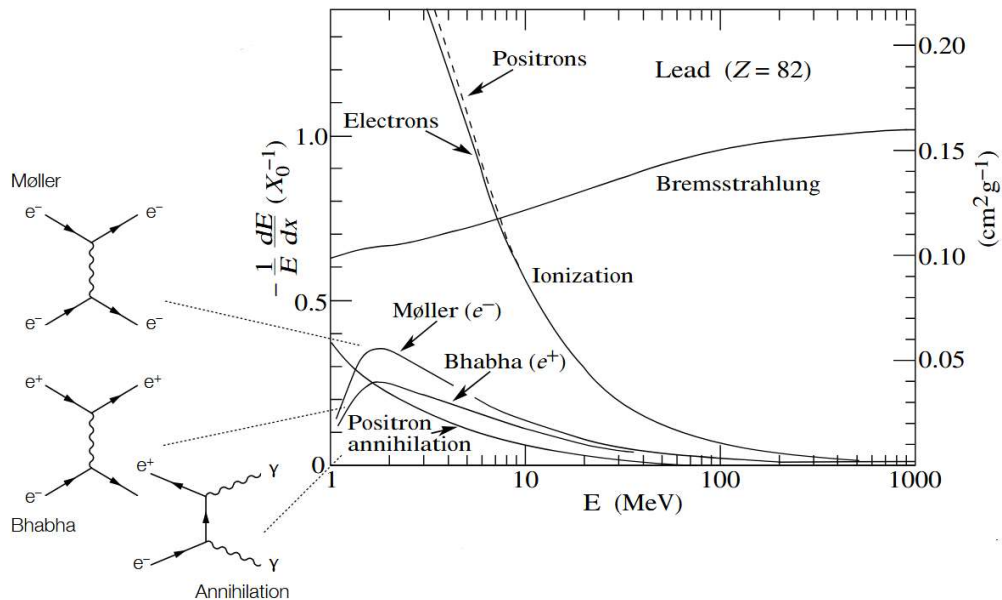


Figure 18. Fractional energy loss per radiation length in the lead as a function of positron or electron energy [58].



Electrons and positrons are negatively and positively charged beta particles. Beta radioactive sources, e.g.  $\text{Sr}^{90}$ , are frequently used to test the detector performance.

### 3.2 pn-junction

The structure and operation principle of pn-junction was described by Shockley in 1949 for the first time [48]. From then it has been widely used in switching, rectification, and for other functions in electronic circuits, including detectors for the High Energy Physics. A pn-junction based upon silicon is created by replacing a tiny amount of the silicon atoms in the crystal with Type-V atoms called donors (e.g. Sb, As, or P), hence creating states (or vacancies) within the forbidden region between the valence and conduction bands. The semiconductor at this point is n-type silicon. P-type silicon is formed similarly: type-III atoms (e.g. Boron) are introduced to semiconductor to replace a tiny amount of the silicon atoms; in this case, Boron atoms are called acceptors. Then semiconductors of two different types are joined, and electrons from the *n*-type side of the semiconductor move to the *p*-type side, while holes from the *p*-side travel to the *n*-side. This process is called carrier diffusion and happens due to the large gradient of carrier concentration at the junction between *p*-side and *n*-side. Mobile holes leave uncompensated negative acceptor ions close to the junction because the acceptors are fixed in the semiconductor lattice. In the same way, a fraction of the positively charged donor ions close to the junction stay uncompensated due to the electrons that moved from the *n*-side. Therefore, a positive space charge is created close the *n*-side of the junction whereas a negative space charge emerges close to the *p*-side. This *space charge region* (also the *depletion region*) is a source of an electric field directed from the positively charged ions to the negative ions. At a certain temperature when no voltage is applied to the diode and no external excitations occur, the hole and electron currents flowing through the junction are equal to zero. It means that for both holes and electrons the drift current caused by the electric field cancels the diffusion current resulting from the gradient of the concentration.

At equilibrium, the total electrostatic potential which is referred to as the *built-in potential* establishes between the *n*-side and the *p*-side regions

$$V_{bi} = \frac{k_B \cdot T}{q} \cdot \ln \left( \frac{N_A \cdot N_D}{n_i^2} \right), \quad (3)$$

where  $V_{bi}$  is a function of concentrations of dopants,  $N_D$  for donors and  $N_A$  for acceptors and in silicon takes a value of  $V_{bi} \simeq 0.7 \text{ V}$ .

The total width  $W$  of the depletion layer depends on the built-in potential as follows

$$W = x_p + x_n = \sqrt{\frac{2 \cdot \varepsilon}{q} \cdot \left( \frac{1}{N_A} + \frac{1}{N_D} \right) \cdot V_{bi}}, \quad (4)$$

where  $x_n$  and  $x_p$  are the width of the depletion region in the  $n$ -side and  $p$ -side respectively, and  $\varepsilon$  is the silicon dielectric constant.

The joint pn-structure can be in three main states: *thermal equilibrium*, *forward biased*, and *reverse biased* (Figure 19).

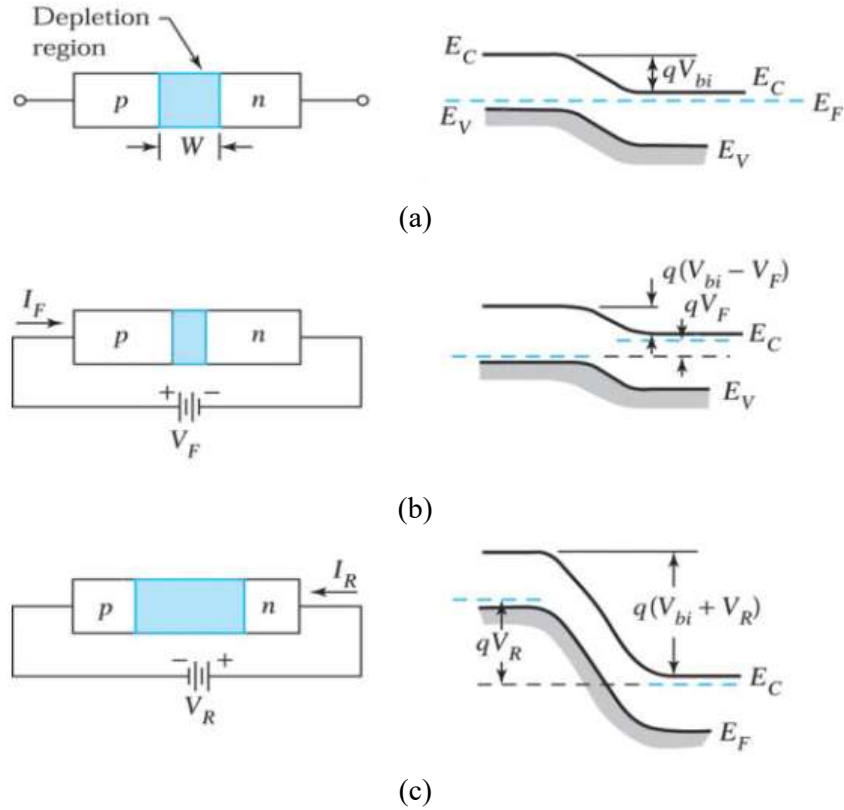


Figure 19. Representations of width of the depletion layer and energy band diagrams for a pn-junction under three biasing states: (a) Thermal-equilibrium; (b) Forward-biased pn-junction; (c) Reverse-biased pn-junction [25]

The pn-junction turns to the reverse-biased state, as illustrated in Figure 19c, if a positive voltage  $V_R$  is applied to the  $n$ -side with respect to the  $p$ -side. In this case full

electrostatic potential applied to the junction raises by  $V_R$  and in equation (4)  $V_{bi}$  is replaced by  $V_{bi} + V_R$ . Reverse bias increases the depletion layer width, which is reflected in a formula:

$$W = x_p + x_n = \sqrt{\frac{2 \cdot \epsilon}{q} \cdot \left( \frac{1}{N_A} + \frac{1}{N_D} \right) \cdot (V_{bi} + V_R)} . \quad (5)$$

Reverse biasing is the main operation mode of the silicon detector.

### 3.3 Working principle of a silicon detector

Semiconductor sensor is based on a pn-junction structure. Depending on the application and the requirements of the detector, it can be designed in different forms: strips, multistrips, pixel, pad detectors. Figure 2.1 shows a sketch of a pixel detector.

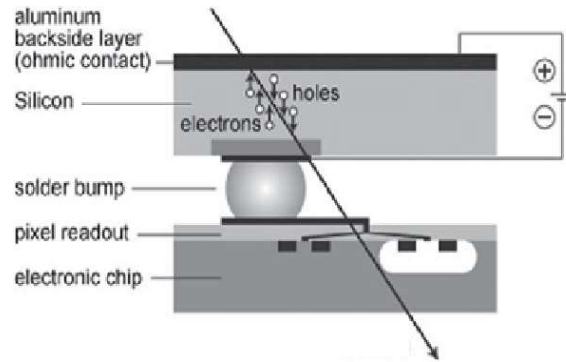


Figure 20. The schematic of a pixel silicon detector [12]

When an external reverse bias is applied to the electrodes, a depleted region and a large electric field are formed. A particle crossing a silicon detector loses energy by ionization and create electron-hole pairs along its path. The generated holes and electrones drift to the electrodes due to the electric field, inducing a signal that can be measured. This signal then proceeds to read-out electronics and can be analyzed.

### 3.4 Shockley-Ramo's theorem and induced current

The signal of a detector is determined by the current induced on the electrodes by moving charge. Even though it is sometimes described as charge collection, the signal appears when the charge just begins to move within the detector and terminates when the full charge is collected (the so-called *charge collection time*). The value of the current induced on an electrode at a certain moment for a charge  $q$  can be estimated using the *Shockley-Ramo's* theorem [29][30]:

$$I = -q \cdot \vec{v}(x) \cdot \vec{E}_w(x), \quad (6)$$

where  $E$  is an electric field between the electrodes,  $v(x)$  is the charge velocity and  $x$  is the charge position between electrodes.  $E_w$  is often referred to as the *weighting* field and defines how the charge couples to the respective electrodes, while the electric field  $E$  defines the charge drift. In mathematical terms, the weighting field is defined by applying a positive unit potential to an electrode, while applying zero potential to the other electrodes with subsequent solving of the Poisson equation. Hence, the weighting field is connected only with the sensor and electrode geometry, the positioning of the electrodes with respect to each other (readout and backplane) and does not rely on the movement of the charges. An illustration of the weighting field for strip and pixel detector geometries is shown in Figure 21.

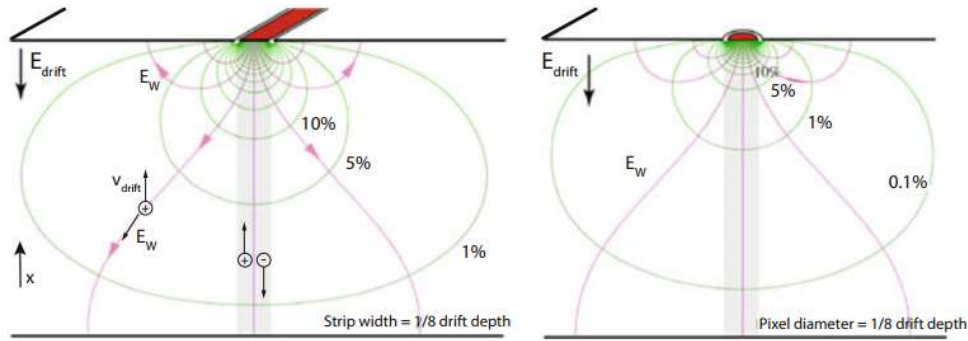


Figure 21. The *lines* represent the weighting potential and weighting field whereas the electric field indicated as a single vector is assumed to be linear throughout the volume of a detector. On the *left* picture a strip detector configuration is shown while a pixel detector geometry is illustrated on the *right* [28]

For a parallel plate sensor geometry when the backplane opposite a single strip, weighting and drift field have an identical form, which means that the weighting field may be not considered separately.

### 3.5 Characteristics of an operating detector

#### Charge transportation and collection

Charge transportation in silicon occurs due to two mechanisms: *drift* and *diffusion*. Free charges drift when one applies an external electric field to the material and both holes and electrons start to move accordingly to their polarities. Carriers acquire a velocity that is proportional to the electric field  $E$ :

$$\vec{v}_e = -\mu_n \vec{E}, \quad (7)$$

$$\vec{v}_h = \mu_p \vec{E}, \quad (8)$$

where the mobilities of electrons  $\mu_n$  and holes  $\mu_p$  have been defined:

$$\mu_n = \frac{q \cdot \tau_n}{m_n}, \quad (9)$$

$$\mu_p = \frac{q \cdot \tau_p}{m_p}, \quad (10)$$

where  $m_p$  and  $m_n$  are the effective masses of holes and electrons;  $q$  is the elementary charge;  $\tau$  is the time interval between two scattering processes at phonons, impurities or crystal defects in the material.

At low electric fields, the mobilities can be considered constant, while at high fields, around  $10^7 \text{ V/cm}$  for silicon at room temperature, mobilities are not anymore proportional to the electric field, and the drift velocities saturate (as shown in Figure 22).

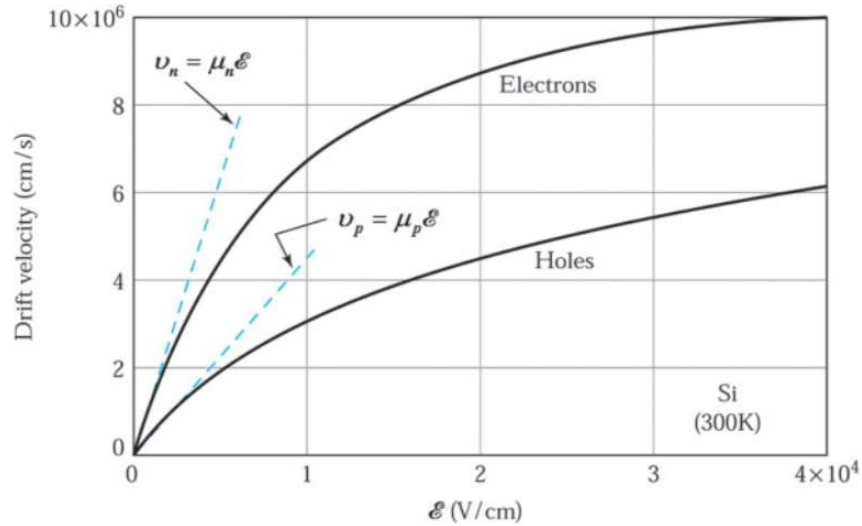


Figure 22. Drift velocity versus electric field in silicon [25]

The total drift current density is given by the sum of the drift currents of electrons and holes:

$$J_{tot}^{drift} = e \cdot (\mu_n \cdot n + \mu_p \cdot p) \cdot E \quad (11)$$

The second type of charge transportation in silicon is *diffusion*. It occurs due to the random movement of charge carriers from the area with a higher concentration of charge carriers to the region with a lower concentration of charge carriers described as a flux. The equations that describe the flux diffusion are:

$$\Phi_n = -D_n \cdot \nabla \cdot n , \quad (12)$$

$$\Phi_p = -D_p \cdot \nabla \cdot p , \quad (13)$$

where  $\Phi_p$  and  $\Phi_n$  are the flux of holes and electrons;  $\nabla \cdot p$  ( $\nabla \cdot n$ ) are the concentration gradients of holes (electrons);  $D$  is the diffusion coefficient connected with mobilities by Einstein's relation:

$$\frac{D_n}{\mu_n} = \frac{k \cdot T}{q} , \quad (14)$$

$$\frac{D_p}{\mu_p} = \frac{k \cdot T}{q} . \quad (15)$$

Combining diffusion and drift, it is possible to obtain the total current density for electrons and holes:

$$J_n = J_n^{drift} + J_n^{diffusion} = q \cdot \mu_n \cdot n \cdot E + q \cdot D_n \cdot \nabla \cdot n , \quad (16)$$

$$J_p = J_p^{drift} + J_p^{diffusion} = q \cdot \mu_p \cdot p \cdot E + q \cdot D_p \cdot \nabla \cdot p . \quad (17)$$

In case of a parallel electrode configuration of a detector, drift velocity is defined by the bias voltage  $V_b$  and the value of an electric field  $E$  as follows

$$v = \mu E = \mu \frac{V_b}{d} . \quad (18)$$

Assuming the weighting field  $E_w$  and electric field  $E$  to remain constant up to the moment when the charge reaches the electrode, the current  $I$  induced on the electrode is:

$$I = -q \cdot v \cdot E_w = -q \cdot \mu \frac{V_b}{d^2} , \quad (19)$$

where  $q$  is the elementary charge;  $d$  is the detector thickness. The current induced by both moving holes and electrons is described by the equation

$$I = -q \cdot E_w \cdot \left( \sum_i v_{i,electrons} + \sum_j v_{j,hole} \right). \quad (20)$$

Assuming  $x$  to be a distance from the anode where an electron-hole pair is created, the charge collection time can be calculated as

$$t_e = \frac{x}{v_e} = \frac{x \cdot d}{\mu_e \cdot V_b} \quad (20)$$

for electrons, and

$$t_h = \frac{d - x}{v_h} = \frac{(d - x) \cdot d}{\mu_h \cdot V_b} \quad (21)$$

for holes.

The total induced charge by the motion of electrons and holes within the detector is

$$Q = \int_0^{t_{e,h}} I(t) dt \quad (22)$$

or, more specifically

$$Q_e = e\mu_n \frac{V_b}{d^2} \frac{x \cdot d}{\mu_e \cdot V_b} = e \cdot \frac{x}{d} \quad (23)$$

for electrons and

$$Q_h = e\mu_h \frac{V_b}{d^2} \frac{(d - x) \cdot d}{\mu_h \cdot V_b} = e \cdot \left(1 - \frac{x}{d}\right) \quad (24)$$

for holes.

The total collected charge  $Q_e + Q_h$  is proportional to the energy deposited by the passage of radiation.

### Capacitance

Another parameter that should be mentioned is the capacitance of a sensor. Due to the fixed charges represented by positive and negative ions on  $n$ -side and  $p$ -side of the pn-junction, the depleted area shows the properties of a parallel-plate capacitor where the width of the depletion layer functions as a spacing between the plates of a capacitor. The width of the depletion region increases with the applied reverse bias, and hence as

for a common capacitor the capacitance reduces. The capacitance *per unit area* can be evaluated with the following expression [25]

$$C = \frac{dQ}{dV} = \frac{dQ}{W \cdot \frac{dQ}{\varepsilon}} = \frac{\varepsilon}{W} \cong \sqrt{\frac{q \cdot \varepsilon \cdot N}{2 \cdot V}}. \quad (25)$$

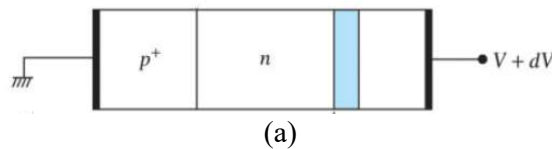
The capacitance-voltage characteristics usually measured for each detector might be used to determine an arbitrary impurity distribution within the detector. The change in a charge  $dQ$  within a depletion layer of a pn-junction shown in Figure 23a when the applied voltage changes by  $dV$  is defined by  $qN(W)dW$  which is indicated as the blue coloured area in Figure 23b. Hence, the change in the voltage  $V$  (blue colored region in Figure 23c) is [25]

$$dV \cong (dE) \cdot W = \left( \frac{dQ}{\varepsilon} \right) \cdot W = \frac{q \cdot N(W) \cdot dW^2}{2 \cdot \varepsilon}. \quad (26)$$

Substituting  $W$  from the equation results in an equation which can be used to define the concentration of an impurity at the edge of the depletion area [25]:

$$N(W) = \frac{2}{q \cdot \varepsilon} \left[ \frac{1}{d(1/C^2)/dV} \right]. \quad (27)$$

Thus, one can measure the capacitance per unit area versus applied voltage and plot  $1/C^2$  versus  $V$ . The slope of the plot  $d(1/C^2)/dV$ , gives  $N(W)$  while the width of a depletion layer  $W$  is determined from the equation (25). A series of such calculations produce a full profile of an impurity distribution. This approach is usually called the *C-V method* for determining impurity profiles, and it will be used in the experimental part of the thesis.





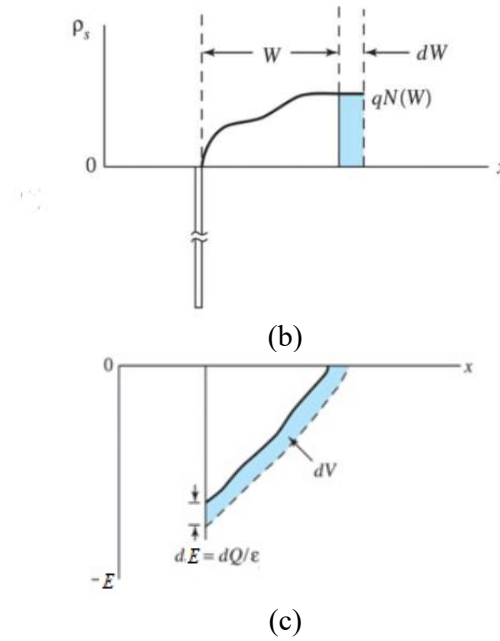


Figure 23. (a)  $p^+-n$  junction with an arbitrary impurity distribution. (b) Change in space charge distribution in the lightly doped side due to a change in applied bias. (c) Corresponding change in electric-field distribution [25]

### Breakdown voltage

The electric field intensity maximum occurs between the n- and p-type semiconductor and can be estimated with the formula [25]

$$\epsilon_{max} \cong \frac{2 \cdot V}{d} = \sqrt{\frac{2 \cdot V \cdot N \cdot q}{\epsilon}} \quad (28)$$

If it increases beyond a critical level, above  $10^6 - 10^7$  V/m, the current begins to flow due to the *Zener breakdown* based on the “tunnel effect” or *avalanche breakdown* happening because of charge multiplication mechanism. Both breakdown processes are reversible and non-destructive if the magnitude of the current is such that the semiconductor does not overheat.

### Leakage current

The current that normally flows if a pn-junction is in a reverse biased state is usually referred to as a leakage current and denoted as  $I_0$ . The current-voltage characteristic

$I(V)$ , the relation between the circulating current and the applied voltage, for a common silicon pn-diode characterized with a leakage current  $I_0$  is

$$I(V) = I_0 \cdot \left( e^{\frac{q \cdot V}{k_B \cdot T}} - 1 \right), \quad (29)$$

while the real behaviour for all voltages is shown in Figure 24.

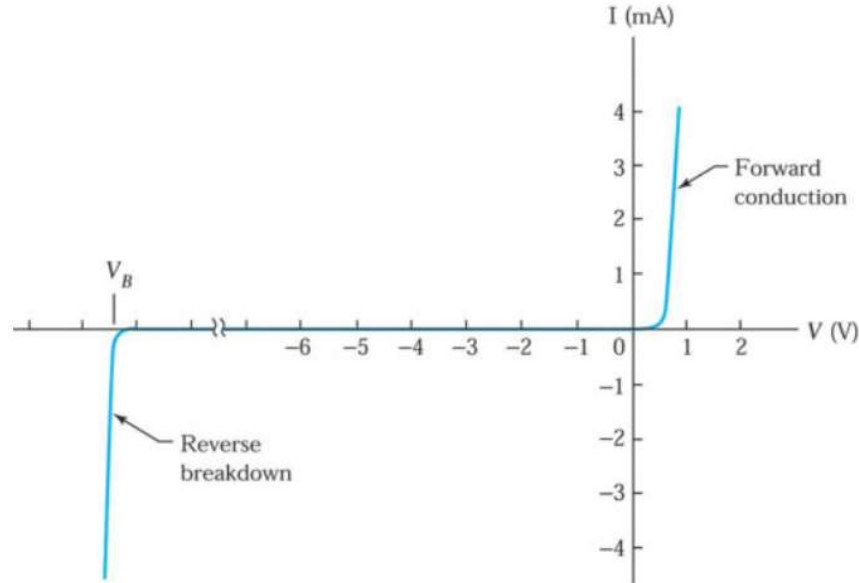


Figure 24. Current-voltage  $I(V)$  characteristics of a common silicon pn-junction [25]

The primary source of *leakage current* is thermally generated electron-hole pairs which cannot recombine because of the electric field applied to the pn-junction, and drift towards the electrodes inducing a current. A second, less important source of leakage current are the minority carriers, namely electrons on  $p$ -side and holes on the  $n$ -side of the junction. When the pn-junction is in a reverse-biased state, they act like the pn-junction is forward biased and therefore they start flowing in the sensor inducing a current.

### Full depletion voltage

When the width of the space charge region  $W$  equals the physical width of the sensor  $d$ ,  $V$  is called the *full depletion voltage*,  $V_{FD}$  [28]:

$$V_{FD} = \frac{d^2}{2 \cdot \epsilon \cdot \mu_n \cdot \rho}. \quad (30)$$

Full depletion voltage describes the minimal operation value, in other words the voltage the detector must sustain without going into the current breakdown. Figure 25 illustrates the need to over-deplete the sensor to collect charges, in case of the  $p$ -in- $n$  detector configuration holes, from the whole volume of a detector and to ensure a faster drift of charge carriers to the electrodes. If full depletion is not reached, the pairs generated in the inactive volume recombine immediately and do not contribute to the signal.

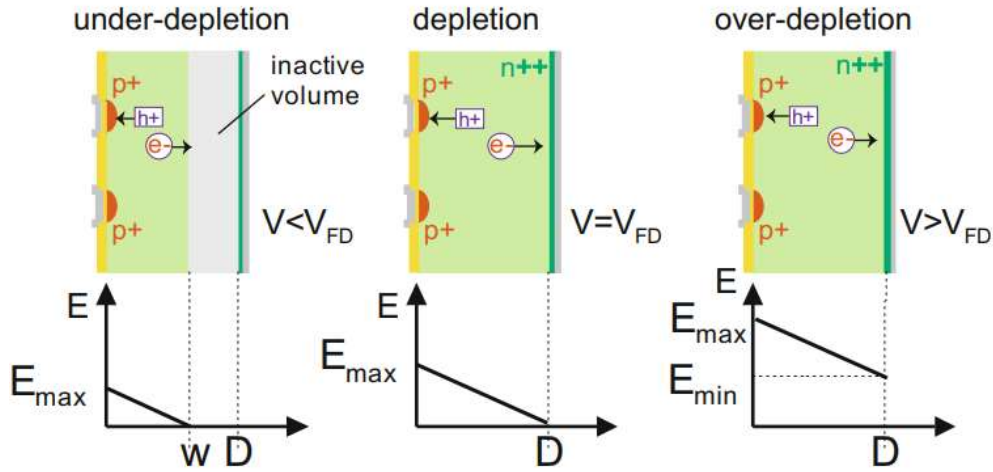


Figure 25. The field in the bulk silicon is linear, depleting a certain volume of a detector. The *left* part of the figure depicts an under-depleted detector ( $V_b < V_{FD}$ ), while the *right* picture shows the over-depletion operation mode ( $V_b > V_{FD}$ ), the picture in the *middle* illustrates full depletion  $V_b = V_{FD}$ . [28]

The depletion voltage can be identified from  $1/C^2$  versus  $V$  characteristic that covers the range of voltages from under-depletion to over-depletion (see Figure 26). The regime when the applied voltage  $V_b$  is less than  $V_{FD}$  is fitted to a straight line of the constant nonzero slope, while the operation mode with the voltage  $V_b$  higher than  $V_{FD}$  is fitted by a straight line with almost zero slope. The intersection of these lines yields  $V_{FD}$ .  $V_{FD}$  depends on the detectors' type and is in the range of tens to hundreds of Volts.

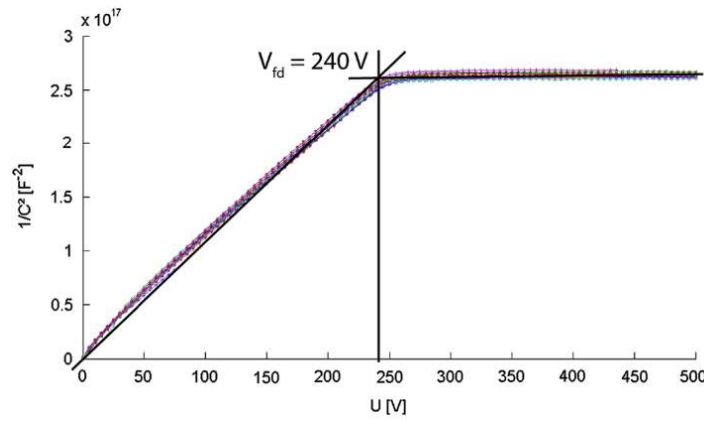


Figure 26. Typical C-V curves for silicon detectors. The full depletion voltage  $V_{FD}$  is extracted from the intersection of two linear fits to the rise and the plateau of the curve [60]

### 3.6 Radiation damage

Detectors are often placed near the particle collision point in the inner region of the CMS, ATLAS, and other experiments. The shift to HL-LHC will boost the particle rate and hence the dose of radiation the tracking devices will be exposed to which affects the performance of the detectors and electronics [66].

Radiation often damage the silicon crystal and triggers atoms in the crystal lattice to change their position. The effect of the radiation changes with the energy of a particle: while charged particles and neutral particles with high energy create cluster deformities, low energy charged particles lead to point defects. Radiation damage could be separated into two types.

The first type of radiation damage is *the bulk damage* (or also *the displacement damage*) resulting from Non-Ionising Energy Loss (NIEL). This usually leads to altering the detector parameters such as the *depletion voltage* caused by extra acceptors settling in the lower half of the bandgap and donors in the lower half, a decline in *charge collection efficiency* as a consequence of holes and electrons trapping, and also a rise of the leakage current (Figure 27).

The second type of radiation damage is *the surface damage* happening because of Ionising Energy Loss (IEL) that leads to the deposition of charges near the oxide structure, usually,  $\text{SiO}_2$  which insulates the layers on the two faces of the detector, or at the Si/ $\text{SiO}_2$  interface. These charge carriers cannot be removed and form local charge

concentrations: these charges can be fixed, trapped or mobile. Surface damage typically leads to alterations in *noise* and *breakdown voltage*.

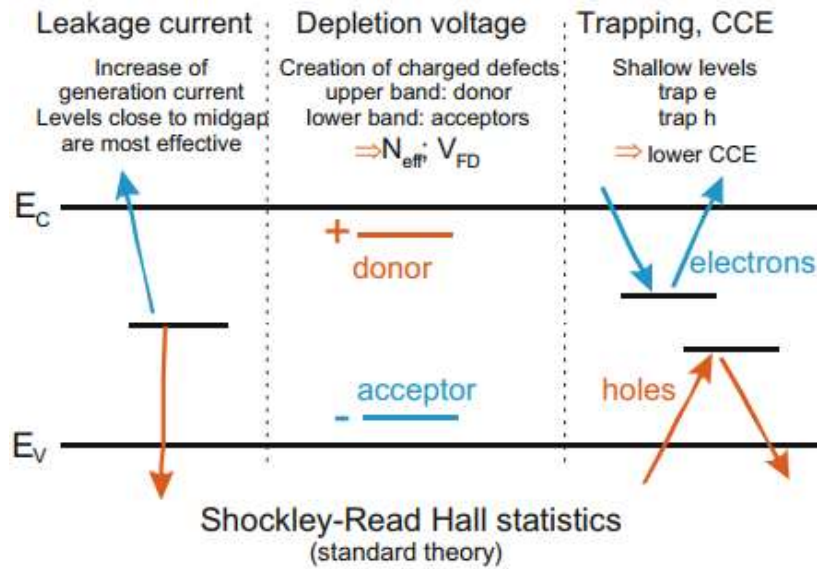


Figure 27. Schematic view of the introduced energy levels due to defects caused by radiation.

Adapted from [28]

Charged particles, then, mostly affect the surface of the detector, while neutral particles (especially low-energy ones) damage the bulk.

## 4 Ultra-Fast Silicon Detectors

Tracking in 4 dimensions demands the engineering of a new segmented silicon sensor with high time resolution and associated electronics. One of the approaches to resolve this problem is to use Ultra-Fast Silicon Detectors (UFSD).

### 4.1 Time Resolution

The time measuring scheme can be replaced with a capacitor ( $C_d$ ) that represents a detector, a current source connected in parallel to the capacitor, and a pre-amplifier that shapes the signal. The time of crossing (or the *time of arrival*) of a particle through the sensor is determined by the time when the output signal  $S$  of the pre-amplifier crosses a given threshold  $V_{th}$  (Figure 28).

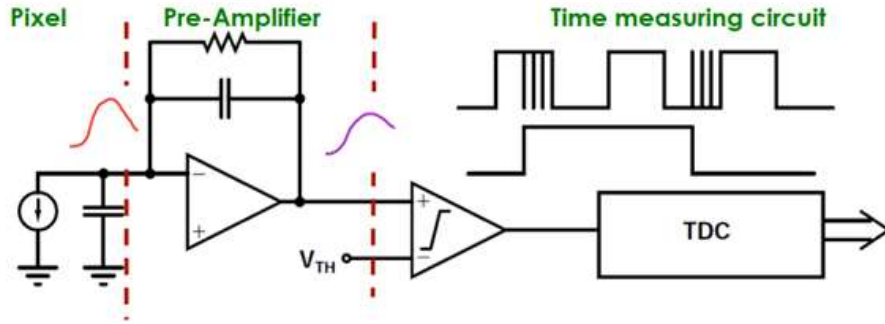


Figure 28. Main structural elements of a timing detector. The time is measured when the signal exceeds the threshold of a comparator [61]

The error on this quantity is the *time resolution*  $\sigma_t$  which is the convolution of several contributions [17]

$$\sigma_t^2 = \sigma_{jitter}^2 + \sigma_{Landau-timewalk}^2 + \sigma_{Landau-noise}^2 + \sigma_{Distortion}^2 + \sigma_{TDC}^2 \quad (31)$$

Due to the importance of these effects on the overall timing performance and the requirements they pose on the development of a timing detector, some of them will be discussed in detail hereafter.

### Jitter

The term  $\sigma_{jitter}$  accounts for the time uncertainty caused by minor fluctuations of the signal that make it cross the comparator threshold earlier or later than it would have without noise, as represented in Figure 29.

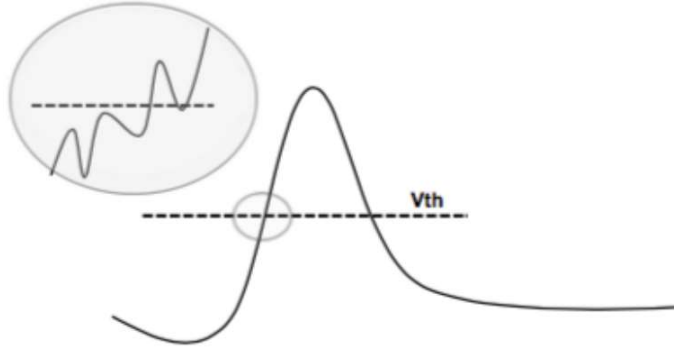


Figure 29. Jitter effect on a threshold discriminator

Jitter is directly proportional to the noise level  $N$  produced within the sensor and/or by the electronics and inversely proportional to the slope of the signal near the value of the comparator threshold:

$$\sigma_{Jitter} \simeq \frac{N}{dV/dt} = \frac{t_{rise}}{S/N} . \quad (32)$$

Therefore, jitter term can be lowered by rising signal magnitude  $S$ , that can be achieved using an internal gain in the detector, or by reducing  $t_{rise}$ . The latter can be reached by decreasing the thickness of the detector, as a thinner detector gives output signals with less  $t_{rise}$  although with the same magnitude as for thicker detectors [15]

### Landau fluctuations

The signal uniformity of silicon detector is limited by the physics governing energy deposition as the distribution of charge generated by an ionizing particle passing a detector fluctuates from one interaction to another. These variations lead to two effects: an overall change in magnitude of a signal, that is the origin of the so-called time walk effect (Figure 30), and fluctuations in a current signal, commonly referred as Landau noise [18]. The pictures on the left side of Figure 31 illustrates two simulated energy depositions of a MIP, whereas on the right side the corresponding total currents and their electron and hole components are depicted for both cases. The variations of the signal amplitude and shape are sufficiently large, and this seriously imposes limits on the time resolution. One way to overcome this issue is using thinner detectors, since their steeper signal is more resistant to signal fluctuation [24].

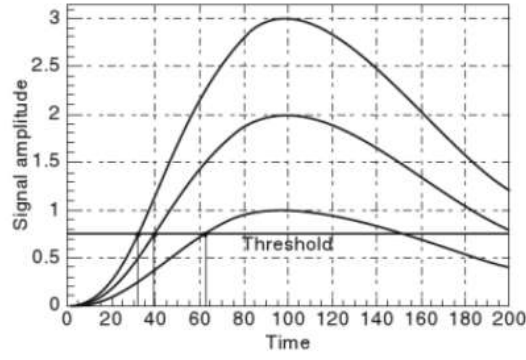


Figure 30. For a given signal increase time, the time at which the amplitude equals the threshold depends on the signal-over-threshold ratio. This effect is called the time walk [62]

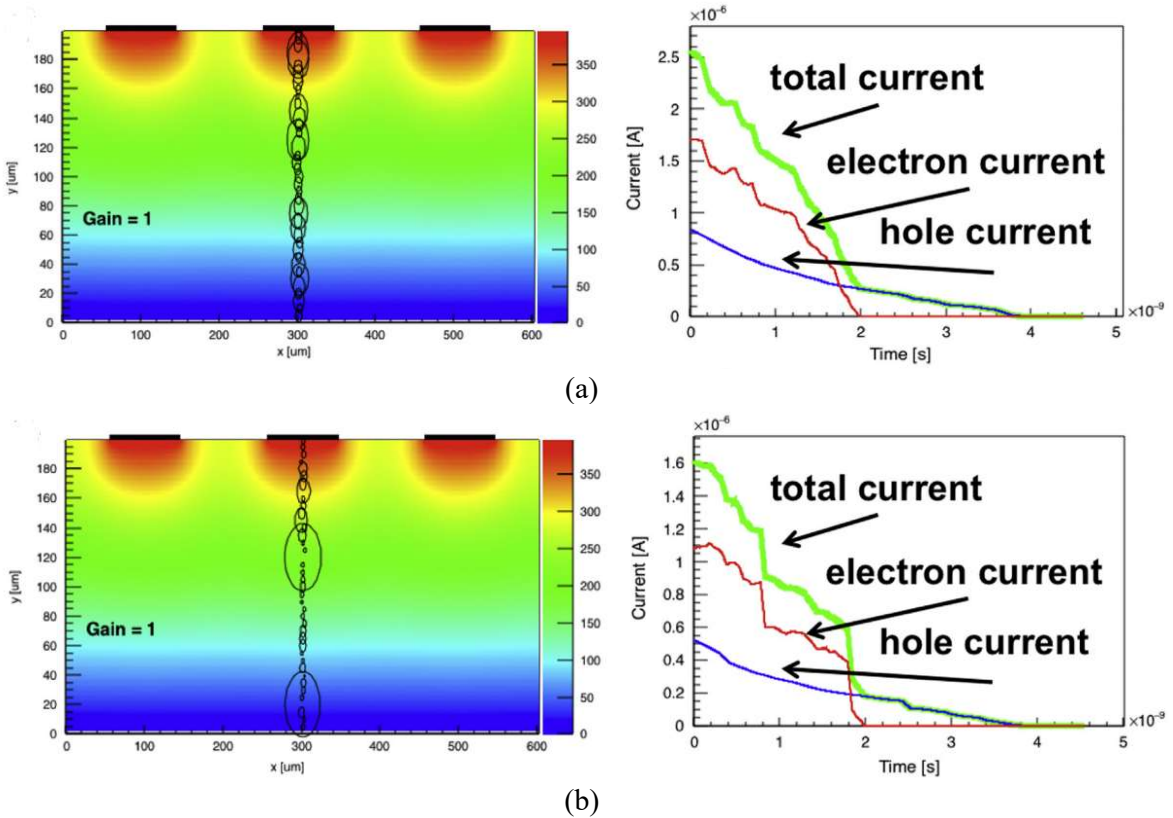


Figure 31. Energy deposits in a silicon detector with gain  $G = 1$  (a), and the corresponding current signals (b) [17]

### Non-uniform weighting field

The term  $\sigma_{Distorsion}$  is created by time fluctuations resulting from the inhomogeneities of the electric field  $E$  in detector influenced by the geometry configuration of the electrodes. The current signal according to the Shockley-Ramo's theorem,



$$i(t) = -q \cdot \vec{v} \cdot \vec{E}_w . \quad (33)$$

To reduce the fluctuations in signal shape, charge velocity  $\vec{v}$  ought to be uniform throughout the whole sensor volume as well as weighting field  $\vec{E}_w$  need to be constant along the sensor pitch. The former requirement is fulfilled by saturating the drift velocity by means of the high electric field (more than  $30 \text{ kV/cm}$  for silicon), whereas the latter is obtained by use of wide strips when the strip pitch is on the same scale as the strip width [17].

The uniformity of the weighting field influences on the coupling of a generated charge to the electrode, which is always should be the same, regardless of the position of the charge. The simulation below shows that for the geometry of the first electrodes, the weighting field is not uniform along the  $x$ -axis of the detector. Therefore the charges generated by particles impinging far from the electrode have a bad coupling with it. On the contrary, the coupling for the second geometry shown on the right side of Figure 32 is better.

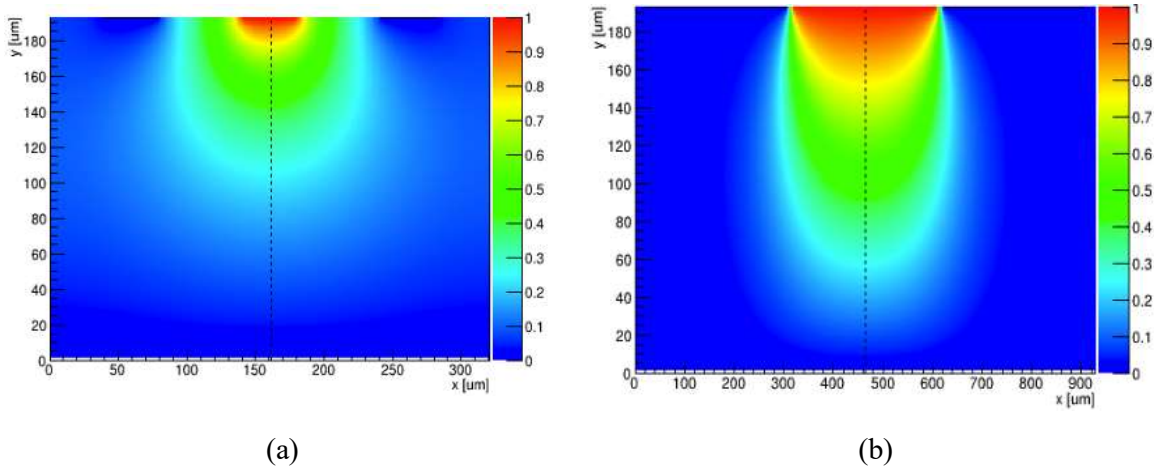


Figure 32. An example of weighting fields generated for a) a strip with  $100 \mu\text{m}$  pitch and  $40 \mu\text{m}$  width, where almost no coupling presents away from the electrode; b) a pixel with  $300 \mu\text{m}$  pitch and  $290 \mu\text{m}$  width, where strong coupling exists almost all the way to the backplane [35]

Planar sensors have an advantage over the 3D sensors in terms of the field uniformity. While former collect charges in implants close to the surface, 3D detectors harvest charges via columns mounted in the detector bulk as shown in Figure 33. For 3D sensors, there are strong theoretical arguments [32] in support of their use as UFSDs

with gain; however, the main problem is that it would be difficult to achieve the homogeneity of the field around the narrow columns.

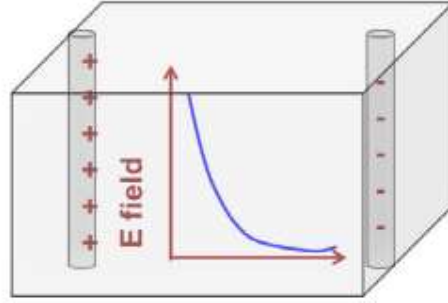


Figure 33. The sketch of the 3D columns. This type of sensors has electric field changing rapidly with the position [15]

### TDC effect on timing resolution

The timing information acquired from the detector needs to be stored for the subsequent readout. Commonly this is done in a *TDC* (Time-to-Digital Converter) where the time of the front edge of the discriminator signal is digitized and placed in a time bin of width  $\Delta T$ , defined by the *TDC* least significant bit. This process will result in the timing uncertainty of  $\Delta T/\sqrt{12}$ , i.e. a bin width of  $\Delta T = 25$  picoseconds leads to a contribution of the *TDC* to the overall timing of about 7 picoseconds [21]. The value of the *TDC* term can be reduced by precise binning of the *TDCs* widely used in high energy physics experiments. For example, with the help of HPTDC [33] method  $\sigma_{TDC}$  can be kept below ten ps, and thus can be negligible comparing to other contributors to an overall detector time resolution.

## 4.2 The structure and working principle of an Ultra-Fast Silicon Detector

The basic  $n^+/p/p^-/p^+$  structure of the UFSD, based on a standard PIN detector, is shown in Figure 33.

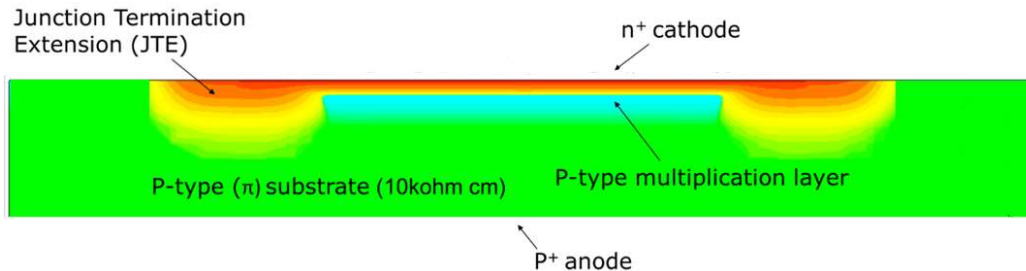


Figure 33. A schematic cross-section of the UFSD pad design [40].

The figure illustrates the main feature of UFSD which is usually referred to as the *multiplication layer* (or also the *gain layer*). It consists of an  $n^+$  cathode with high doping concentration of  $10^{19} \text{ cm}^{-3}$  and a p-type area with  $10^{16} \text{ cm}^{-3}$  doping concentration under it [40]. The material of a bulk is a p-type silicon with high resistivity. An extra  $n^+$  doped area is introduced to decrease the amplitude of the electric field along the edges of the cathode. It is called the Junction Terminating Extension or JTE and discussed in more detail later. An example of the doping concentration through the n-type cathode and p-type multiplication implant is shown in Figure 34.

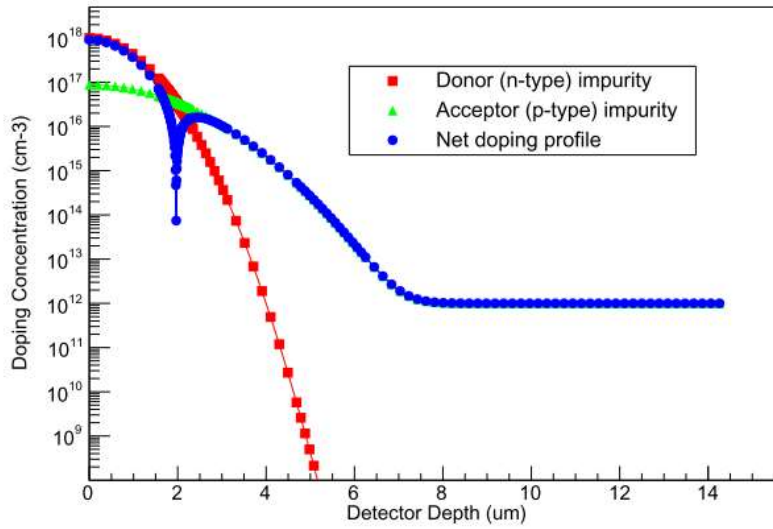


Figure 34. Typical 1D doping profile of both acceptor and donor concentration and the sum of the two is shown [34]

The processes occurring in n-on-p LGAD can be described as follows:

1. The particle is crossing the sensor and producing electron-hole pairs by ionization;
2. Due to the reverse applied bias, holes drift towards the p-side and electrons to the p-side;
3. When electrons travel across the  $p^+$  multiplication layer they experience a high electric field;
4. This field is responsible for the impact ionization, which produces an avalanche multiplication of secondary charges;
5. Now the total current is due to the additional avalanche contribution

6. The result is an amplified current pulse that is mostly determined by the motion of the holes through the whole thickness of the substrate.

Figure 35 depicts output signals obtained with LGAD and a PIN diode in blue and orange correspondingly. The shape of waveforms varies considerably because of avalanche mechanism existing within the LGAD. In the very beginning, the signals are the same since the drift of electrons depends mostly on the electric field in the bulk of the detector, that is equal both for PIN and LGAD. The distinctions appear just behind the kink in the LGAD signal when multiplication process of electrons takes effect. The pulse indicates as well when a drift of holes to the backside of a detector happens; it occurs after incoming electrons have generated electron-hole pairs via impact ionisation.

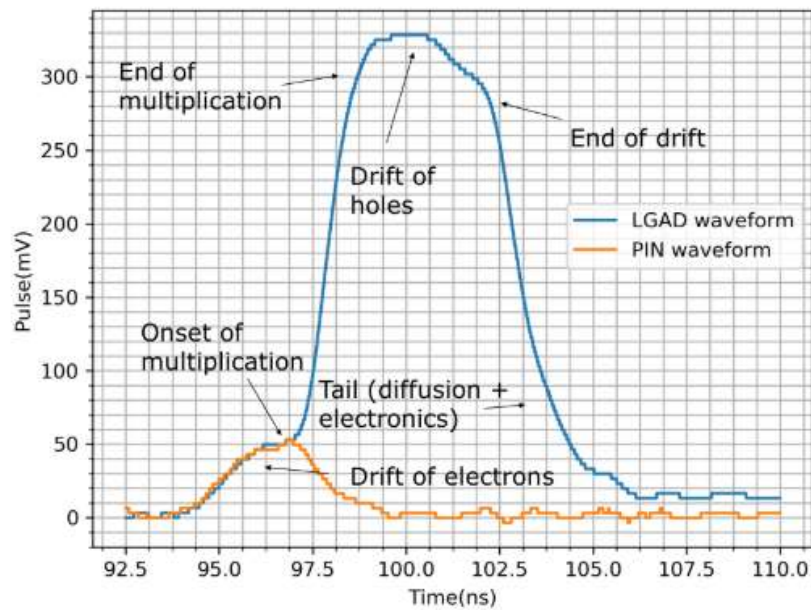


Figure 35. Comparison of signals obtained for PIN and LGAD diodes in orange and blue correspondingly [40]

These pulses, increased by 10-20 times, are fast and are able to offset the small number of charges created by MIP in the thin detector comparing to a common 300 micrometer thick detector. Keeping the gain value significantly below the level corresponding to the avalanche operation mode of a detector, allow the noise to stay low [35].

### 4.3 The multiplication mechanism

Although charge multiplication mechanism may lead to an electrical breakdown in poorly designed semiconductor devices, this process can be utilized in a controlled manner for signal amplification, as in the case of UFSDs.

Charge multiplication in silicon sensors happens when hole or electron is produced in, or is taken into, an area with high electric field within a semiconductor and then is accelerated to a velocity which is enough to create an additional electron-hole pair.

The possibility of generating secondary pairs for holes and electrons is different. By adjusting the electric field, a specific condition can be found when only one type of charge carrier (electrons in silicon) generates secondary charge carriers. At this point, the charge produced via multiplication processes will be proportional to the primary generated charge. It is possible to describe the multiplication of  $N_0$  initial electrons drifting through a silicon path length  $x$  with high electric field with a simple exponential law:

$$N(x) = N_0 \cdot e^{\alpha x} = N_0 \cdot G, \quad (34)$$

where  $G = e^{\alpha x}$  is the gain as a function of  $\alpha(E)$ , the impact ionisation rate, also called the *first Townsend coefficient*, which expresses the amount of electron-hole pairs produced per unit length by a drifting electron.

The ionization rate  $\alpha$  depends on the probability for the carriers to reach this threshold energy, which in general is not only a function of the local electrical field. As a first approximation, a dependence of the  $\alpha$  factor on the electric field is also described as exponential according to the *Chynoweth law* [36]:

$$\alpha_{e,h}(E) = \gamma \cdot \alpha_{e,h}(\infty) \cdot \exp\left(-\frac{\gamma \cdot \beta_{e,h}}{|E|}\right), \quad (35)$$

where  $\beta_{e,h}$  and  $\alpha_{e,h}(\infty)$  are constants for holes and electrons, and  $\gamma$  is a constant which does not depend on the charge carrier nature.

The internal gain of a UFSD detector depend on the temperature through the carriers saturated velocities [37] and the impact ionization rates, which is related to the

reciprocal of the mean free path of the carriers and hence in strong relation with the temperature. With the increase in temperature, the probability for the carriers to achieve the threshold energy for ionization becomes smaller, and the applied external voltage for which the avalanche is uncontrollable increases.

Several empirical models have attempted to express the dependence of the impact ionization rate as a function of the temperature: Van Overstraeten-de Man Model [36], Massey model [39], Okuto-Crowell model [38].

#### 4.4 Irradiation effects and shot noise

Shot noise appears when charge carriers overcome a potential barrier in semiconductor devices, particularly in silicon detectors. If the integration time of an electronics equals  $\tau$ , the equivalent noise charge can be expressed by the following formula [17]:

$$ENC_{Shot} = \sqrt{I_{bulk}/(2q) \cdot \tau}, \quad (35)$$

where  $I_{bulk}$  is the leakage current produced in bulk of a device which then collected by the read-out electrode. For UFSD, this effect is increased by the internal gain, and due to this, shot noise might be a considerable issue and a major source of the noise. Furthermore, since multiplication process is stochastic some carriers multiply more than others, which eventually leads to a further increasing of a noise; this effect is usually referred to as *excess noise factor (ENF)*. The equation for shot noise that considers *ENF* in semiconductor device with a gain is [17]:

$$ENC_{Shot} = \sqrt{\frac{I_{bulk} \cdot G^2 \cdot G^x}{2q} \cdot \tau}, \quad (36)$$

where  $x$  is the excess noise index and  $G$  is value of a gain.

*ENF* results in a quite specific feature: with the gain rising the signal-to-noise ratio ( $S/N$ ) becomes smaller as the signal grows slower than the shot noise. Consequently, to achieve a beneficial effect from the multiplication mechanism, a value of a gain should be small enough (less than 20) to provide an increase of the signal while the shot noise is less than the electronic noise level, as shown in Figure 36.

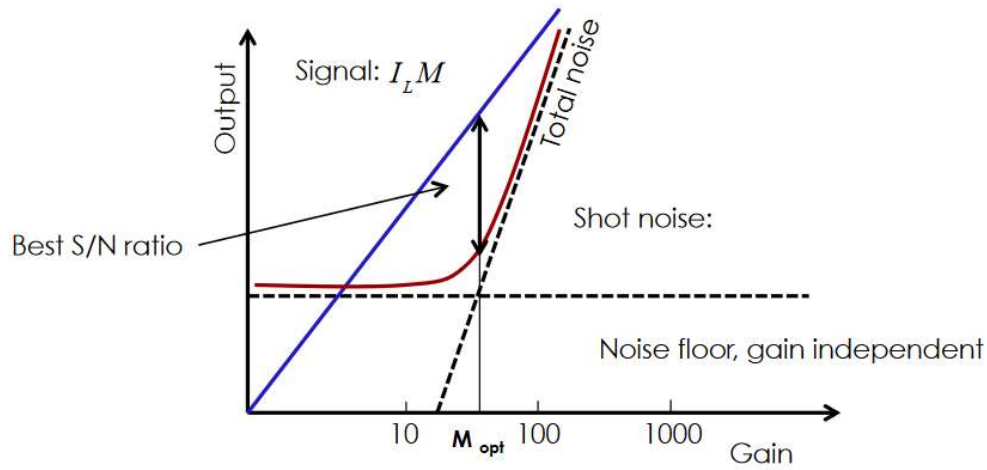


Figure 36. With increasing the gain, the total noise (brown line) rises faster than the signal (blue line), and the S/N ratio worsens. There is an optimum gain value between 10 and 20 [31]

Figure 37 illustrates the influence of gain on shot noise as a function of radiation dose for a four mm<sup>2</sup> 50-micron thick silicon sensor for a two nanosecond integration time; the electronic noise is assumed to be 450 ENC. For irradiated detectors with internal gain shot noise is dominating source of noise. It is considered that small volumes of a detector help to reduce the shot noise if the gain value is kept low enough.

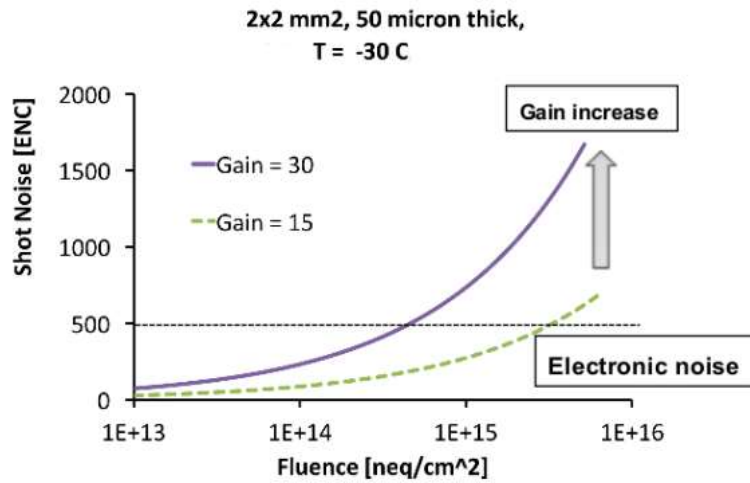


Figure 37. Shot noise increase as a function of fluence for two different gain values [17]

To sum up, the most valuable points to ensure superior time resolution are:

1. electric field to sufficient to saturate velocity and minimize signal distortion,
2. parallel plate detector configuration, providing uniform weighting and electric fields,

3. small volumes, to minimize leakage current and consequently shot noise
4. charge carriers able to obtain high velocity, resulting in large  $dV/dt$ ,
5. low capacitance, to minimize noise and hence jitter term,

Two additional features arise from the UFSD design: low gain (in the order of 10-20) and thin sensors that leads to maximum slew rate  $dV/dt$ , low leakage current and small charge carriers trapping.

#### 4.5 FBK Ultra-Fast Silicon Detectors campaign

The Ultra-Fast Silicon Detectors (UFSD) project was launched in 2015 to develop silicon detectors for 4D tracking with excellent time resolution in the order of tens of picoseconds and space resolution reaching tens of micrometres simultaneously. Low Gain Avalanche Diodes (LGAD) are used as a baseline sensor technology for 4D tracking [45]. These detectors are planned to be used for the upgrade of CMS and ATLAS experiments, to cope with the events overlapping in space. In this section, a review of the progress in technology and configuration of UFSD sensors, engineered at the Fondazione Bruno Kessler (FBK) is presented.

FBK outlines several features of LGADs suitable for timing measurements:

1. signals produced by detector are fast and large enough to provide accurate timing measurements while keeping the noise level almost unchanged (reduced  $\sigma_{jitter}$  term);
2. a pad size of the LGAD is of the order of 1-3 mm<sup>2</sup>
3. a uniform weighting field within the entire sensors' thickness;
4. minimized Landau fluctuations due to small detector thickness (50 microns);

The origins of the listed factors were discussed earlier.

The development of LGADs by FBK within the UFSD project started in 2016. From then on, four UFSD series were released, each of which covered specific features of R&D work required to complete the goals of the project.



In 2016 the first (UFSD1) 300  $\mu\text{m}$  thick LGADs on 6" wafers with five different doses of the gain layer implant were fabricated to adjust the doping concentration of the gain layer, that mainly determines the gain value of the detector; first irradiation tests were performed as well. The sample with higher gain showed time resolution of 55 picoseconds at high reverse bias voltage [20]. The obtained results were very promising taking into account that a relatively thick substrate has been used in this first production.

The aim of the second (UFSD2) run in 2017 was the fabrication of 50  $\mu\text{m}$  thick detectors, with different acceptors in different gain splits, at two different diffusion temperatures, and in multiple structure variations. Both Boron and Gallium acceptor dopants with Carbon co-implantation was used to enhance radiation tolerance. The application of Ga and C dopants has been proposed within the RD50 collaboration to mitigate the disappearance of the gain layer that results from radiation damage. Carbon decreases the concentration of interstitials available for capturing B atoms during irradiation [43], whereas Gallium replacing B minimizes the formation of the acceptor-interstitial [44]. The total test batch consisted of 19 wafers where 10 were with B at two different diffusion temperatures, five different gain splits, with and without C at two different concentrations, and nine wafers with Ga with the same splits of B samples. Each wafer contained several structures (see Figure 38): high granularity multipixel, multipad, single pads, strips, microstrip detectors.

In the fall of 2018, FBK manufactured the third batch of LGADs (UFSD3) to optimize the Carbon concentration fine splitting, the pixel border to improve the fill factor, pixel design and checked the gain uniformity for CMS ETL prototype.

An internal FBK run (UFSD3.1) in June of 2019 was dedicated to the study of the origin of early breakdown and «pop-corn» noise observed in UFSD3, due to a combination of very aggressive edge design and incorrect p-stop doping.

The properties of the samples from the last batch of FBK UFSDs are investigated in this thesis.

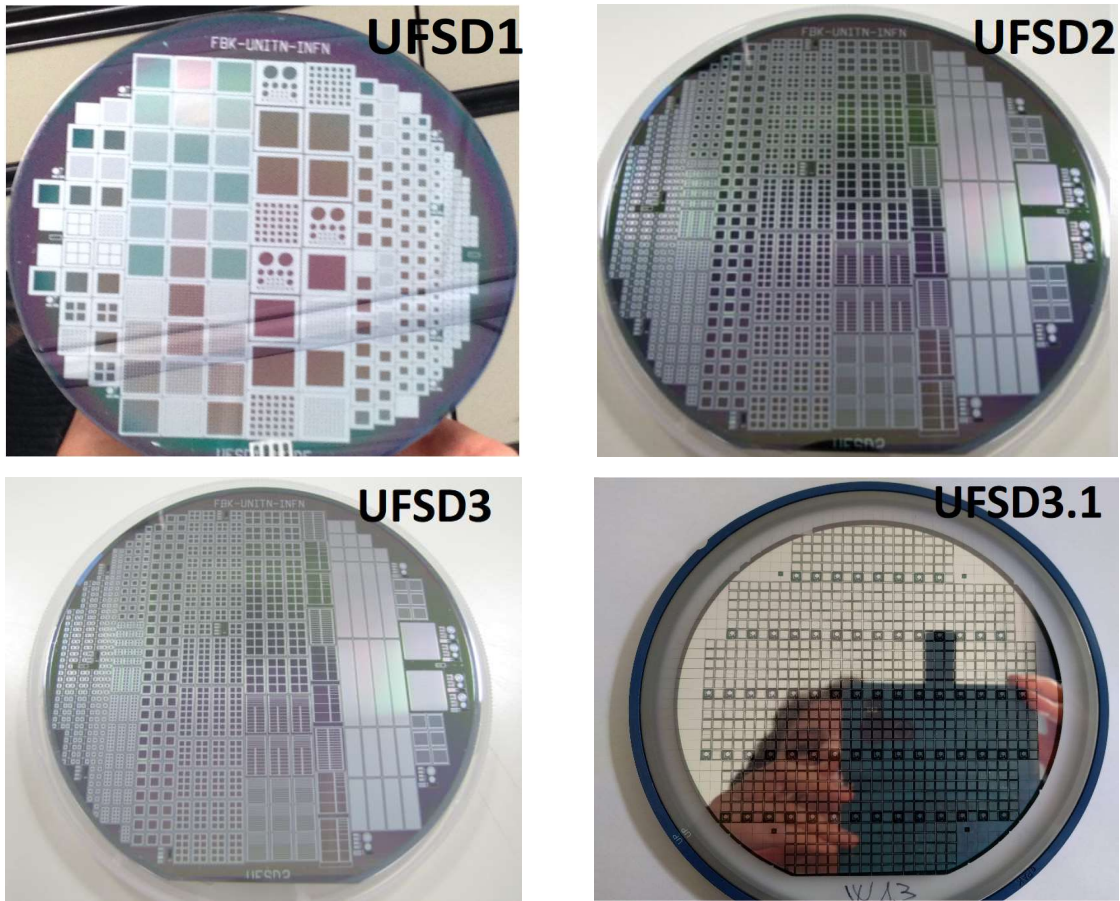


Figure 38. Photos of 4 different FBK UFSD productions [45]

#### 4.6 FBK Ultra-Fast Silicon Detector performance

This paragraph contains a brief overview and comparison of the performance of the UFSD series, and also includes the description of UFSD parameters such as the uniformity of the gain, time resolution and radiation hardness.

##### The uniformity of the gain

The gain layer doping should be as uniform as possible to make use of the detectors in large area UFSD sensors. It has been shown that a subtle difference of one percent in doping concentration shifts the operating bias voltage to up to 15 V depending on the configuration of the gain layer. Hence, the non-uniformity should be kept below one percent for a single detector, to have sensors with similar performance which at the same time can properly share the bias voltage with adjusting sensors.

The uniformity of the gain layer is usually tested by performing capacitance-voltage measurements for a whole batch of pad detectors and consequent analysis of the

$1/C^2(V)$  curves. The voltage at which the gain layer is depleted,  $V_{GL}$ , is proportional to the active acceptor density  $N_A$  in the gain layer [23]. The relative spread of  $V_{GL}$  characterizes the non-uniformity of the gain layer, and it is in the range from two to three percent for the last FBK UFSD series.

### Radiation hardness

Charged particles and neutrons decrease the gain value of the UFSDs, thus affecting the sensor performance; it results from deactivation of the acceptors located in the gain layer region, because of an initial acceptor removal mechanism. The latter is described with an expression:

$$\rho_A(\Phi) = \rho_A(0) \cdot e^{-c \cdot \Phi}, \quad (37)$$

where  $\Phi$  is the irradiation fluence,  $\rho_A(0)$  and  $\rho_A(\Phi)$  are the initial (after a fluence  $\Phi$ ) acceptor density and the density after a fluence  $\Phi$ , and  $c$  is the acceptor removal coefficient depending on the initial acceptor concentration  $\rho_A(0)$  and on the type of irradiation [23].

FBK constantly attempts to improve a radiation resistance of the gain layer, exploring various techniques to create the gain layer, such as adjustment of doping profile and/or type of acceptor and introducing carbon to the gain layer. Figure 39 shows the fraction of the acceptor density in the gain layer surviving at a certain fluence with respect to the fluence received, for several UFSD configurations.

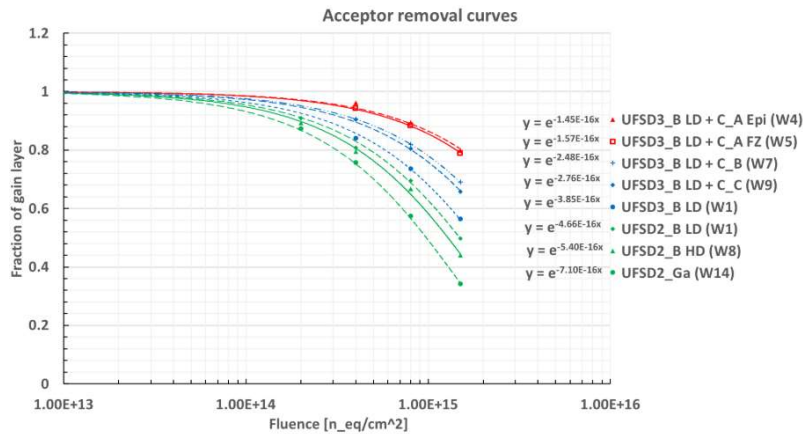


Figure 39. The fraction of the active acceptor density in the gain layer with respect to the fluence received for UFSD sensors with different gain layer configuration. Data points are fitted with an exponential curve  $y = e^{-cx}$ . Smaller coefficient  $c$  leads to more radiation-resistant gain layers [45]

These measurements demonstrate that the most radiation resistant gain layer was manufactured in Low Diffusion (LD - narrower layer profile) with a  $C_A$  dose of carbon.

### Time resolution

The plot depicted in Figure 40 gives an overview of the UFSD time performance. The results for three UFSD sensors are shown, including new and irradiated up to  $3 \cdot 10^{15} \text{ 1MeV/cm}^2$ . The irradiated sensors achieve a given gain for progressively higher bias voltages. A time resolution in the 25-30 ps range, for 50 microns thick UFSD, has been reached for new devices with the perfectly adjusted design of the gain layer, and it is possible to reach a 30-35 ps time resolution when the bias is high enough nearly saturate the holes' drift velocity.

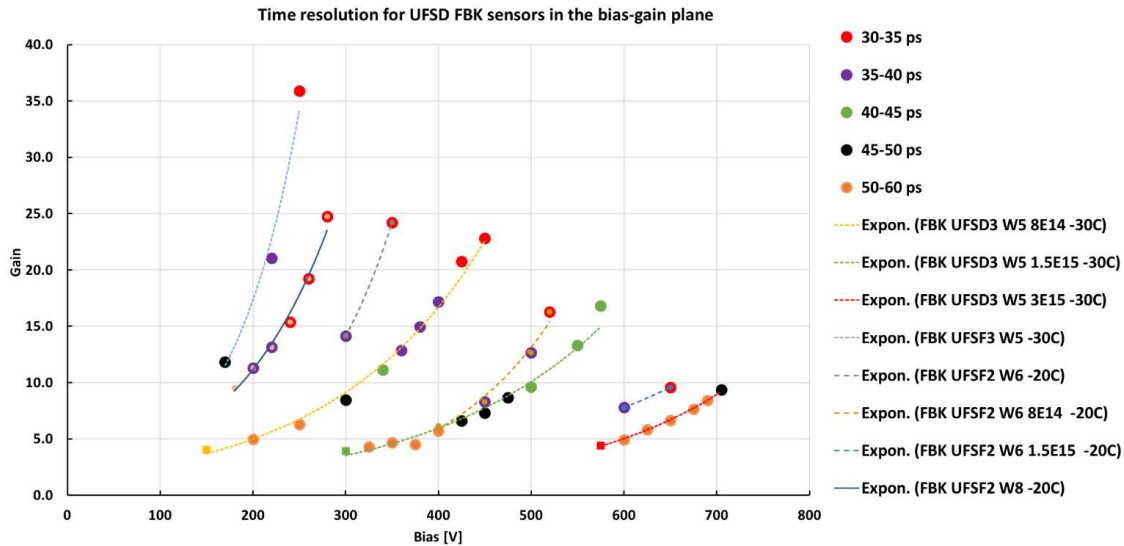


Figure 40. The dependence of gain value on bias voltage for a few FBK sensors, new and irradiated at various fluences. The markers define the time resolution values obtained in laboratory measurements with a  $\beta$ -source, at -20 or -30°C [45]

### Inter-pad gap and fill factor

The multiplication junction requires several guard structures to prevent premature breakdown and reduce the leakage current, especially for detectors exposed to high radiation dose.

The first type of a guard structure currently used in UFSD design is called the Junction Termination Extension (JTE). It is made of a deep  $n^+$  region. Each gain layer of a pad detector is surrounded by a JTE, as shown in Figure 41.

The first reason for introducing a JTE to the UFSD structure is to decrease the magnitude of the electric field on the periphery of a gain layer, that is represented in Figure 41b.

The other reason of implementing such protection structure is to ensure that the electron-hole pairs produced by a particle incident in the area between pad detectors are not reaching the multiplication layer resulting in an out-of-time signal, but absorbed on the pad detector edges by the JTE.

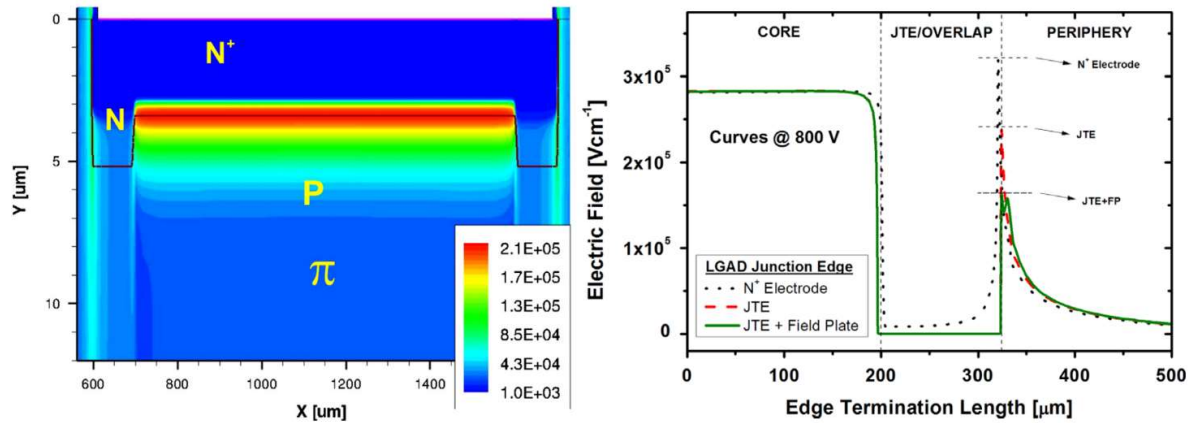


Figure 41. Two-dimensional distribution of the electric field in UFSD (on the left) and the effect of implementing the JTE on the value of the electric field on the periphery of the  $p^+n$ -junction (on the right) [47]

The other guard structure used in UFSD is called the p-stop. The  $\text{SiO}_2$  layer which covers the surface of a silicon detector represents a fixed positive charge. Due to this, an electron accumulation layer which compromises the isolation of pixels can be formed underneath the  $\text{SiO}_2$ . This situation is shown in the upper part of Figure 42. The p-type implant provides fixed negative charges which interrupt the electron accumulation layer and compensate for the positive oxide charge of the  $\text{SiO}_2$ .

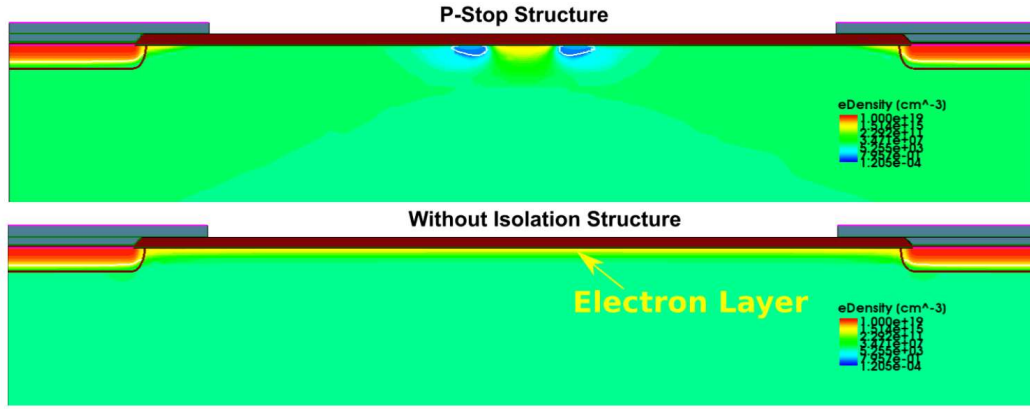


Figure 42. The effect of implementing the p-stop structure on the electron layer under  $\text{SiO}_2$  [63]

In addition to the JTE and the p-stop, a multiple guard-ring termination structure on the side of a gain implant is used to prevent early breakdown at the edges. The structure represents a set of floating  $n^+$  implants with electrodes (Figure 43). The first ring, the closest to the core region of the detector, is grounded to collect the charge carriers created outside the detector and hence reducing the leakage current.

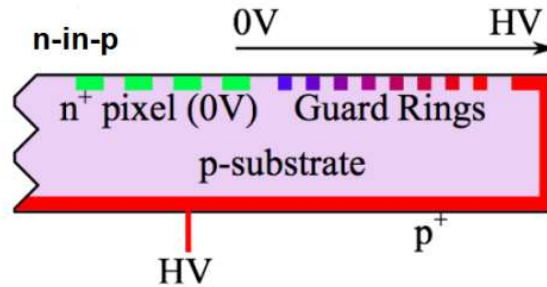


Figure 43. A schematic of the guard rings structure

The proposed configuration results in an area with an absent gain for signal collection, because of the inter-pad gap between the two gain layers, and to an additional periphery of the gain implant where the charges are collected by the JTE without crossing the gain layer (Figure 44).

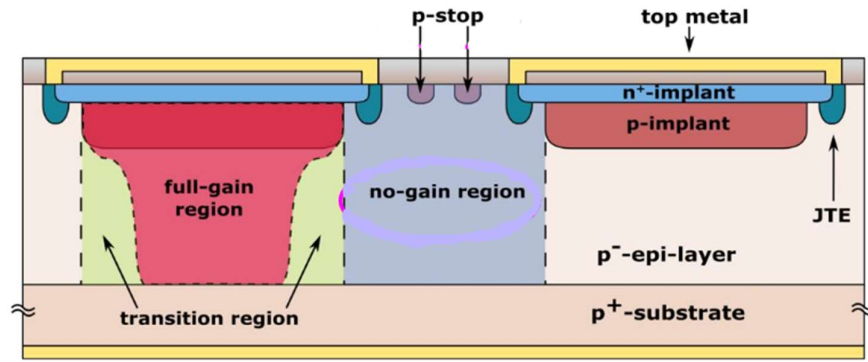


Figure 44. The cross-section of LGAD with marked gain and no-gain regions [63]

The size of the inter-pad no-gain area influences on a sensor array *fill factor*, determined as the ratio of a pad detector sensitive area to its total area. For example, a no-gain area of 40 microns results in a fill factor of 94% (36%) for a 1.3 mm (100 microns) pitch sensor array. Constant attempts are made to increase the fill factor. The inter-pad gap is also one of the factors affecting the breakdown voltage of a pad detector which will be considered in the experimental part of the thesis.



## 5 Experimental part

### 5.1 Measured Sensors

All the tested sensors during the work of this thesis belong to the 2019 production of 50  $\mu\text{m}$  thick UFSDs manufactured by FBK. The tested sensors are 2·2 array of pad detectors with  $1.3 \cdot 1.3 \text{ mm}^2$  area each, shown in Figure 45. Pad detectors have a light-sensitive area surrounded by five guard rings. The sketch of the device cross-section is presented in Figure 46.

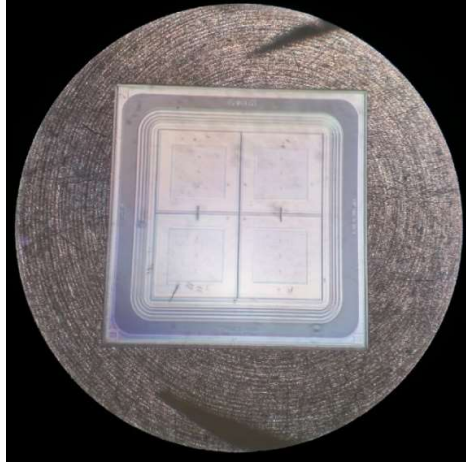


Figure 45. One of measured UFSD3.1 detector

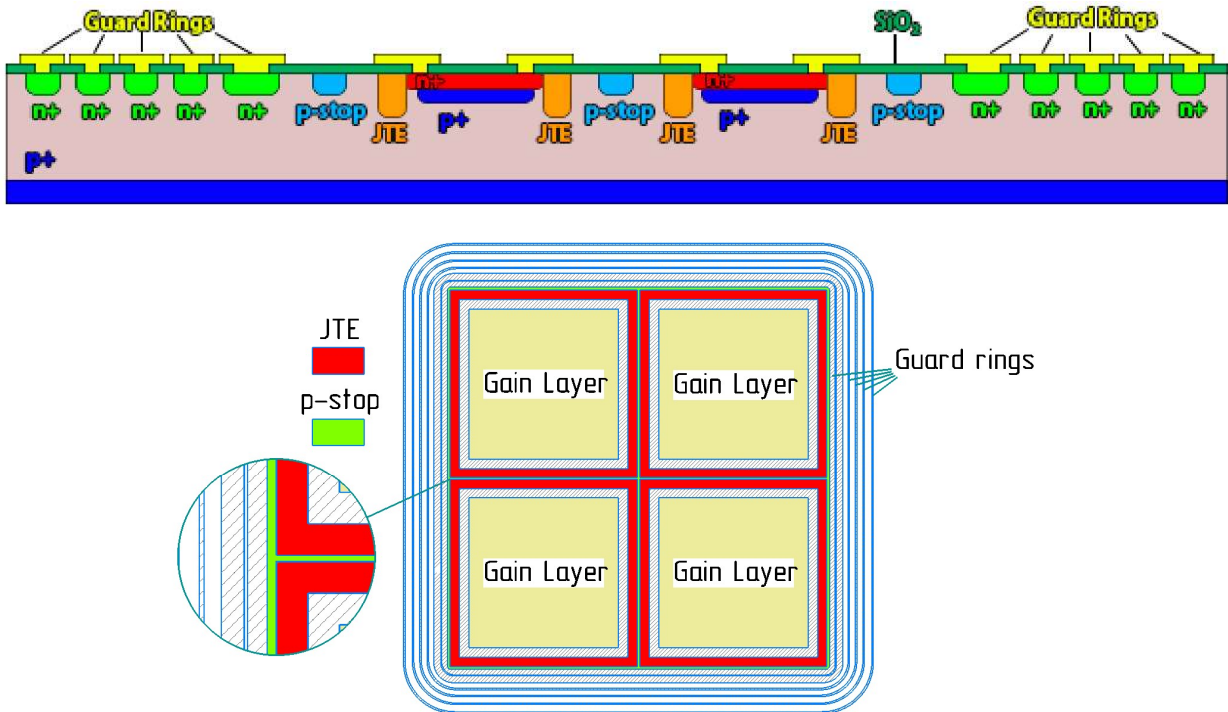


Figure 46. The sketch of cross-section of the measured sensors (NB it is not to scale) and an overall view of the detector from above with indicated JTE and p-stop



During the FBK USFD3.1 production campaign 11 sensor “types” with various properties, which are outlined in Table 1, were fabricated. Sensors have different inter-pad widths and p-stop designs. The tested sensors were based on two wafers W13 and W14, which are characterized by two different concentrations of the acceptors in the p-stop region and the same Boron doping concentration in the multiplication layer.

Considering Table 1, we can conclude that the developers chose three significant factors to study:  $n \cdot F$  - the concentration of acceptors in the p-stop (second column), the width of the inter-pad gap (column 4) and the layout of inter-pad design (column 5). The latter factor has no numerical value and is expressed qualitatively. Column 6 refers to the second factor and is a characteristic of the chosen strategy to enhance the fill factor of the sensor.

Table 1 - List of the measured devices from the FBK UFSD3.1 production. F - FBK scale factor

Wafer	p-stop dose, a.u.	Type	Nominal inter-pad width, $\mu\text{m}$	Inter-pad design	Strategy
W13	$1/20 \cdot F$	1	16	grid + extra grid	Aggressive
		2	21	grid	Medium
		3	21	grid	
		4	24	grid	Safe
		5	25	grid	
		6	28	grid + extra grid	
		7	28	grid + extra grid	
		8	28	grid + extra grid	
		9	38	2 p-stop	Super safe
		10	49	2 p-stop + bias grid	
		11	21	grid	Medium

Table 1 - List of the measured devices from the FBK UFSD3.1 production. F - FBK scale factor (cont.)

W14	$1/10 \cdot F$	1	16	grid + extra grid	Aggressive
		2	21	grid	Medium
		3	21	grid	
		4	24	grid	Safe
		5	25	grid	
		6	28	grid + extra grid	
		7	28	grid + extra grid	
		8	28	grid + extra grid	
		9	38	2 p-stop	Super safe
		10	49	2 p-stop + bias grid	
		11	21	grid	Medium

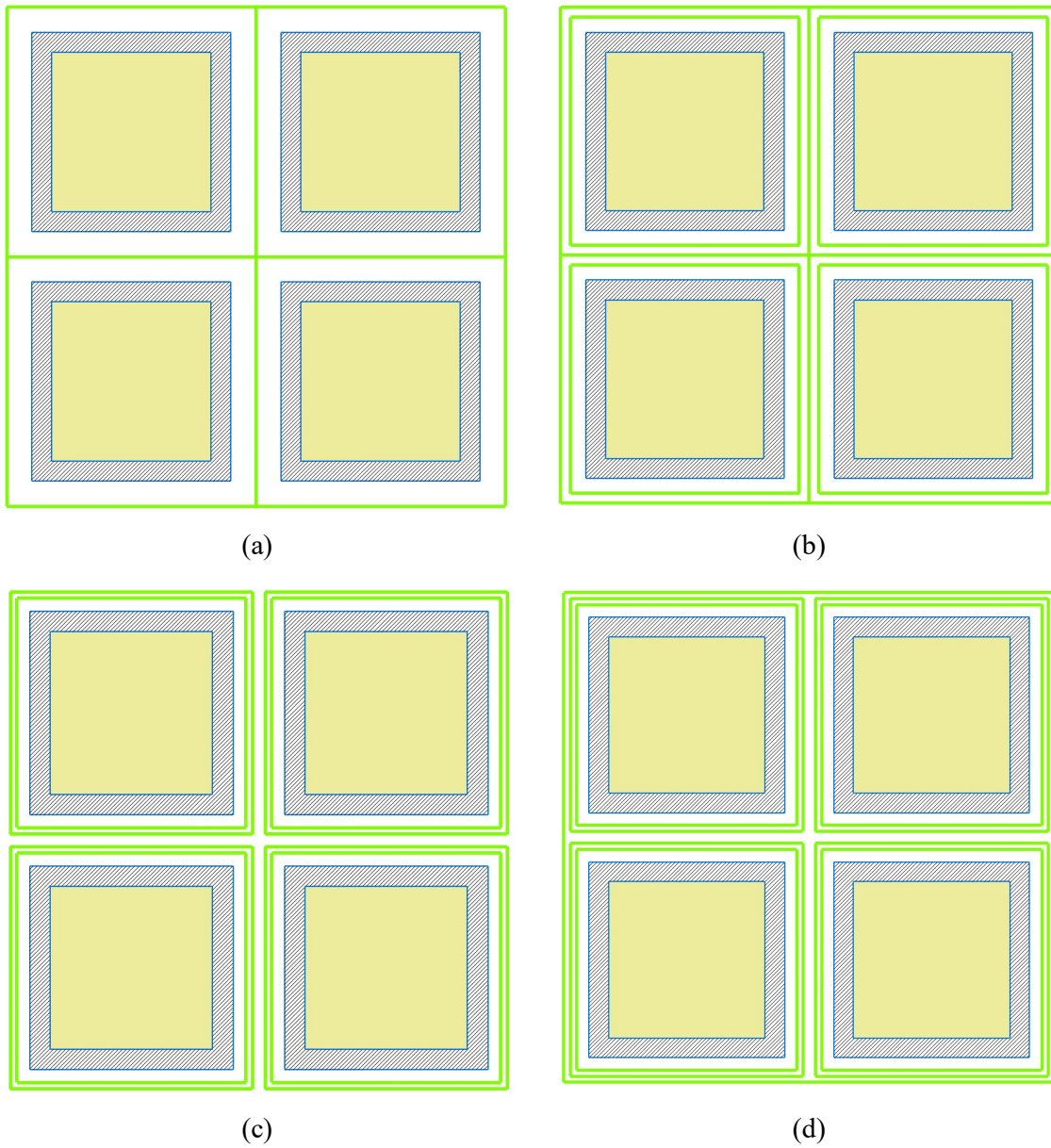


Figure 47. Sketches of FBK inter-pad designs layout: (a) grid; (b) grid and extra grid; (c) 2 p-stop; (d) 2 p-stop and bias grid. P-stops are marked in green color. Inter-pad gaps are not to scale, and guard rings are not shown

## 5.2 Measurement set-up

Characterizing the electrical properties of sensors is fundamental for the evaluation of their quality and performance. To characterize the devices under study in this thesis, two methods were employed: I-V measurements, i.e. leakage current as a function of voltage and CV measurements, i.e. capacitance as a function of voltage. From I-V curves the breakdown voltage, the magnitude of leakage current and power consumption can be determined. C-V curves provide information about the effective doping concentration and the depletion voltage of the sensors.

The main components of the set-up are Karl Süss PM8 probe station (Figure 48), Keithley 2410 source-meter, Keithley 6487 picoammeter, Agilent HP-E4980A LCR meter, Isobox, switch box, banana connectors, chuck, micromanipulators, probe needles and microscope. The measurements are done by setting initial parameters such as frequency, initial and final voltage with steps as well as the number of measurements per step and compliance current on a PC running with a user interface based on MATLAB.

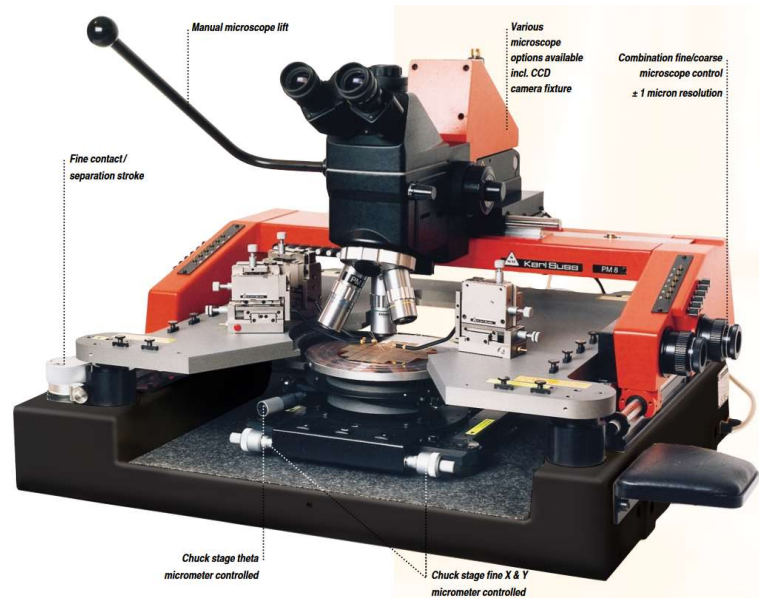


Figure 48. Probe station Karl Süss PM8 photo [64]

In this set-up, the sensor is mounted on a chuck of the probe station which provides the bias voltage from the backplane of the sensor. To ensure that the sensor does not move, it is held through suction by a vacuum pump. All probe needles have a metal tip and

are attached to a micromanipulator by probe holder. The micromanipulator helps in making contact on the pads and guard rings by moving the tip of a probe needle in three dimensions (-x, -y and -z directions) by the help of fine adjustment screws (Figure 49).

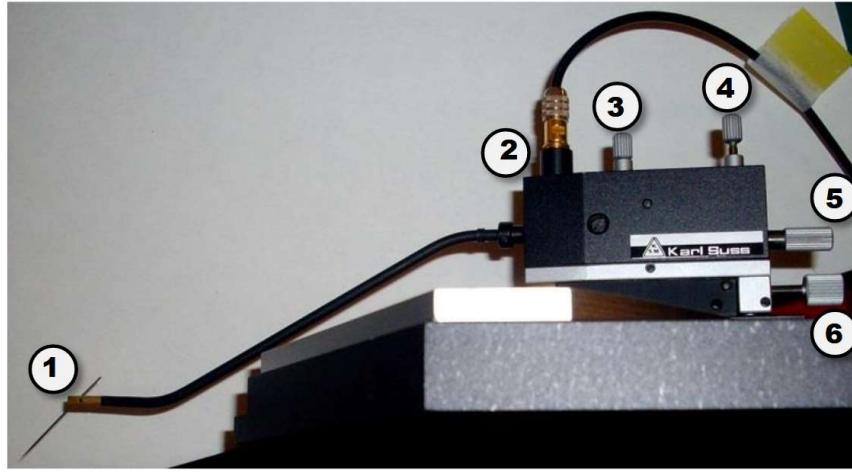


Figure 49. Micromanipulator photo: 1 - the needle; 2 - electric connector; 3 - knob for adjusting the force; 4 - knob for vertical movement; 5 - knob for horizontal movement; 6 - knob for horizontal movement.

To prevent the micromanipulators from moving, they are held by the magnetic force between stage and the base of the micromanipulator. The whole probe station is located inside a Faraday cage that also acts as a dark box, to stop light from interfering with IV measurements. All measurements were performed at the room temperature.

Figure 50 shows the schematics for I-V measurements. There are five needles, one is used to read the current from the pad, the second is connected to the guard ring of the sensor, while other 3 needles are used to ground pads adjacent to the main pad (Figure 51). High voltage to the chuck is applied by the Keithley 2410 source-meter that can provide voltage within the range of  $\pm 1000V$ . The voltage source has a maximum current of 1 mA and can also measure higher currents. It also consists of an electrometer which is completely isolated from the voltage source and can measure current within an accuracy of 100 pA. The probe needle, connected to the guard ring, is grounded with a common ground of the picoammeter and high voltage source. On the other hand, the micromanipulator is grounded through Keithley 6487 picoampere-meter. Keithley 6487 is used to measure the pad current while Keithley 2410 is used to measure the total current.

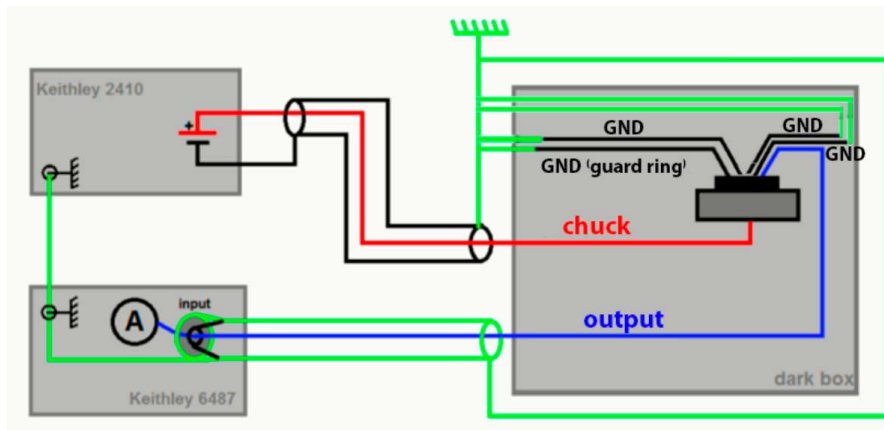


Figure 50. Schematic view of I-V set-up. Adapted from [65]

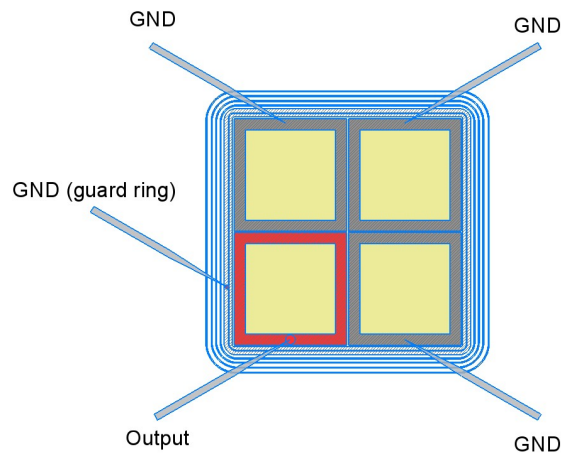


Figure 51. Probe needles placement in “0 pads floating” configuration: four needles are connected to the ground, while the fifth needle is used to read the current from a pad

Figure 52 shows the schematics of the capacitance-voltage measurements. The capacitance measurements are performed using two simultaneous voltage sources: Keithley 2410 is a DC voltage source, while an Agilent HP-E4980A LCR meter provides an AC voltage signal that is swept in time, as shown in Figure 53; LCR meter is connected between the bias line and the backplane through the Isobox. The purpose of the DC voltage bias is to allow sampling of the silicon detector at different depths, whereas the LCR meter provides the small-signal bias so the capacitance measurement can be performed at a given depth in the device.

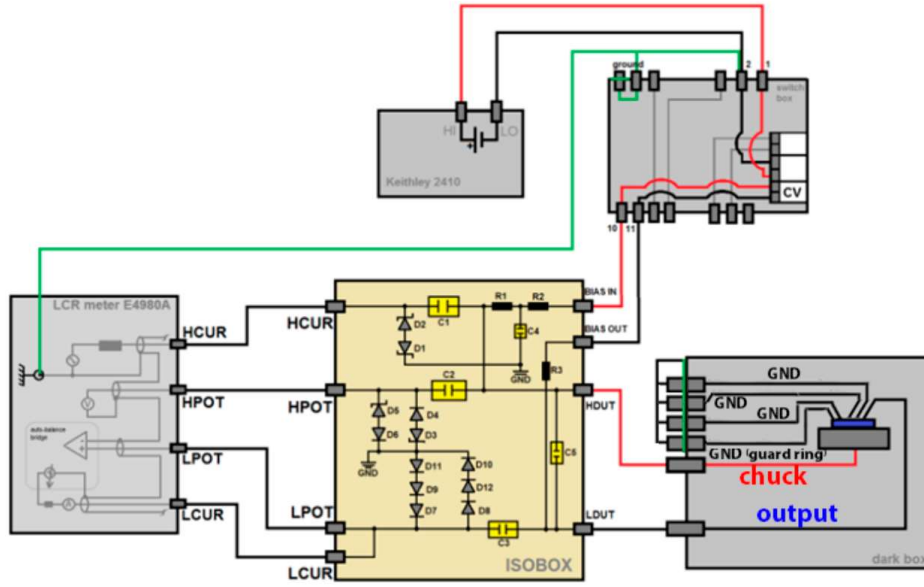


Figure 52. Schematic view of C-V set-up. Adapted from [65]

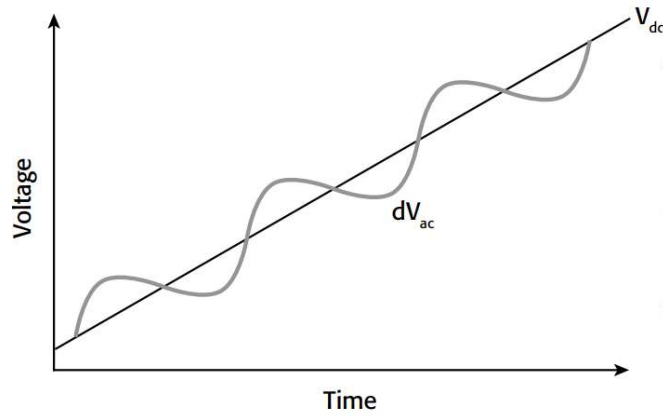


Figure 53. AC and DC voltage of C-V Sweep Measurement

An LCR meter (for inductance  $L$ , capacitance  $C$  and resistance  $R$ ) supplies an AC voltage out of the high current terminal ( $HCUR$ ) and measures the voltage across the detector by the low and high potential terminals ( $LPOT$  and  $HPOT$ ). The current through the device is measured by the low current terminal ( $LCUR$ ). The measured current is integrated over time to derive the change in charge  $\Delta Q$  occurring in the detector due to the change in voltage  $\Delta V$ , and then capacitance  $C$  is calculated as follows:

$$C \equiv \frac{\Delta Q}{\Delta V}. \quad (38)$$

Another important equipment used in the C-V characterization is the Isobox. The Isobox is a circuit board consisting of a range of resistors, capacitors, junction diodes and Zener diodes. The isolation box allows the bias voltage to be applied to the same sample while keeping it out of the LCR meter; at the same time, it isolates the bias-voltage supply from the high-frequency test AC signal. It is assumed that there is DC path through the LCR meter to allow the high-voltage-blocking capacitor to charge and discharge as the bias voltage is slowly varied.

### 5.3 Results

At the first stage, I-V characteristics of all sensors were measured. The measurements of the breakdown voltage as a function of floating pads were performed by contacting the pads and the guard ring with probe needles and then rising needles from one and three pads (Figure 51).

For the convenience of further comparison and analysis, the current-voltage characteristics of all sensors which are based on the same wafer, W13 (the first group), are summarized in one plot (Figure 51). Similarly, the current-voltage characteristics of all sensors of the second group are presented in one plot (Figure 52).

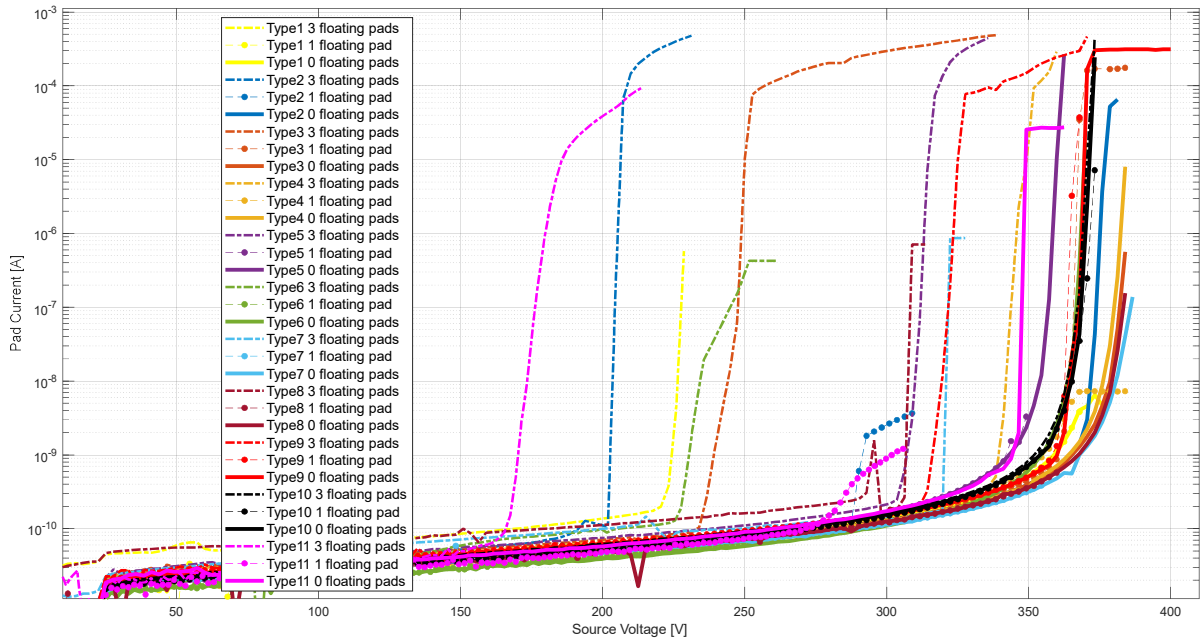


Figure 51. I-V characteristics for W13 sensors. The measurements were taken in three different probe needles configuration with guard ring grounded



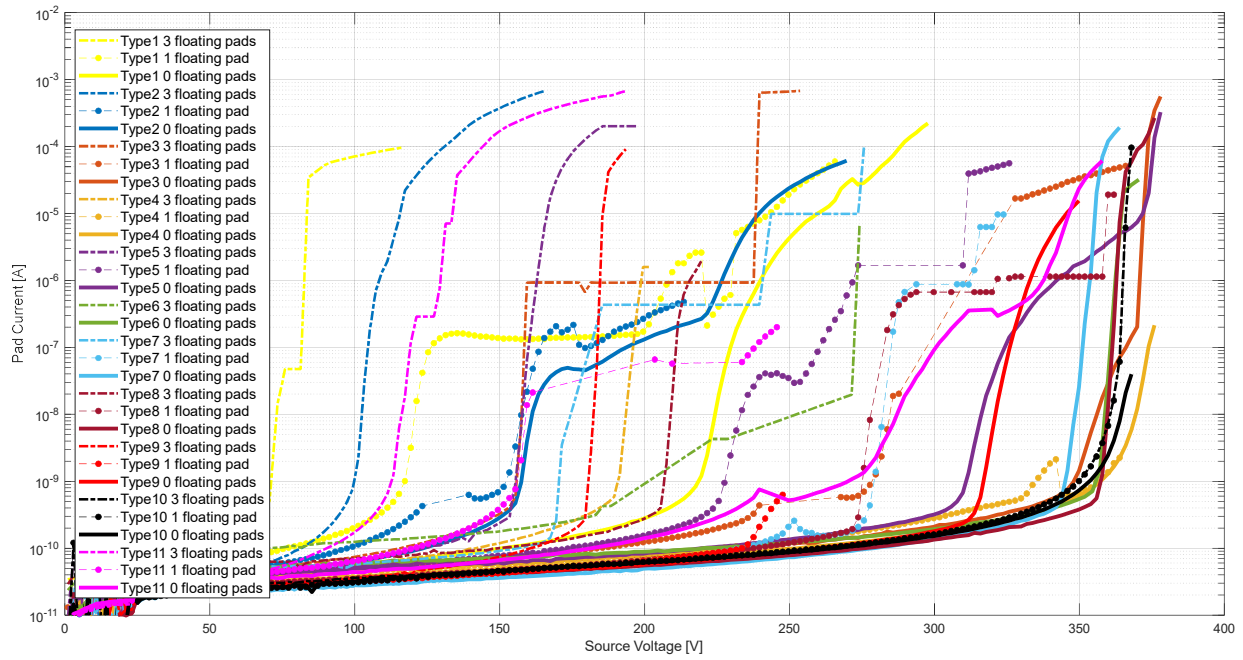


Figure 52. I-V characteristics for W14 sensors. The measurements were taken in three different probe needles configuration with guard ring grounded

The breakdown voltage is determined, as illustrated in Figure 53.

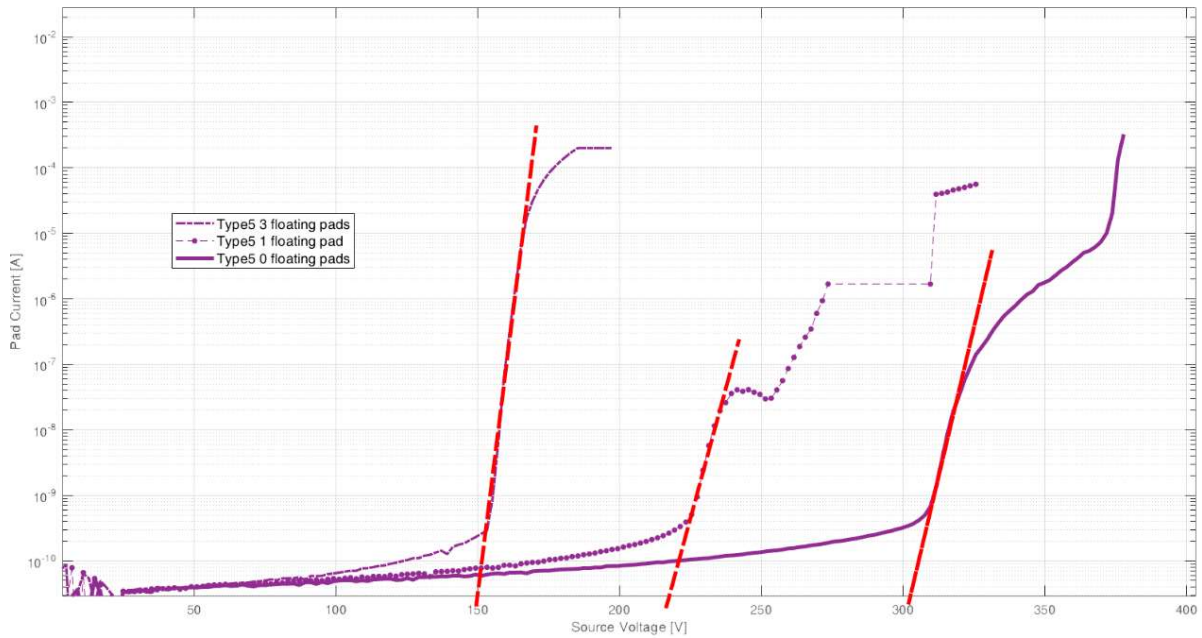


Figure 53. The intersections of the red lines with x-axis give the values of the breakdown voltage

Table 2 and Table 3 report the values of breakdown voltage corresponding to Figures 54 and 55. The first column of the table indicates the type of sensor, while other columns contain the values of breakdown voltage in case of three floating pads, one floating pad and when none of the pads is floating, respectively.

Table 2 - The values of the breakdown voltage for sensors based on W13

Sensor type	$V_{BD}, V$ (3 pads floating)	$V_{BD}, V$ (1 pad floating)	$V_{BD}, V$ (0 pads floating)
Type 1	221	353	353
Type 2	202	293	371
Type 3	234	355	370
Type 4	338	350	370
Type 5	304	333	355
Type 6	228	266	360
Type 7	320	355	365
Type 8	306	360	370
Type 9	312	357	357
Type 10	363	360	360
Type 11	167	278	338

Table 3 - The values of the breakdown voltage for sensors based on W14

Sensor type	$V_{BD}, V$ (3 pads floating)	$V_{BD}, V$ (1 pad floating)	$V_{BD}, V$ (0 pads floating)
Type 1	61	115	210
Type 2	87	151	152
Type 3	111	278	342
Type 4	177	342	362
Type 5	150	223	305
Type 6	183	-	352
Type 7	167	276	342
Type 8	206	272	356
Type 9	177	236	312
Type 10	354	360	360
Type 11	110	150	250

The C-V scans acquired at 1 kHz frequency for  $1.3 \cdot 1.3 \text{ mm}^2$  pads belonging to 13 and 14 wafers are reported in Figures 54 and 55. The measurements were taken in “0 pads floating” configuration with guard ring grounded.

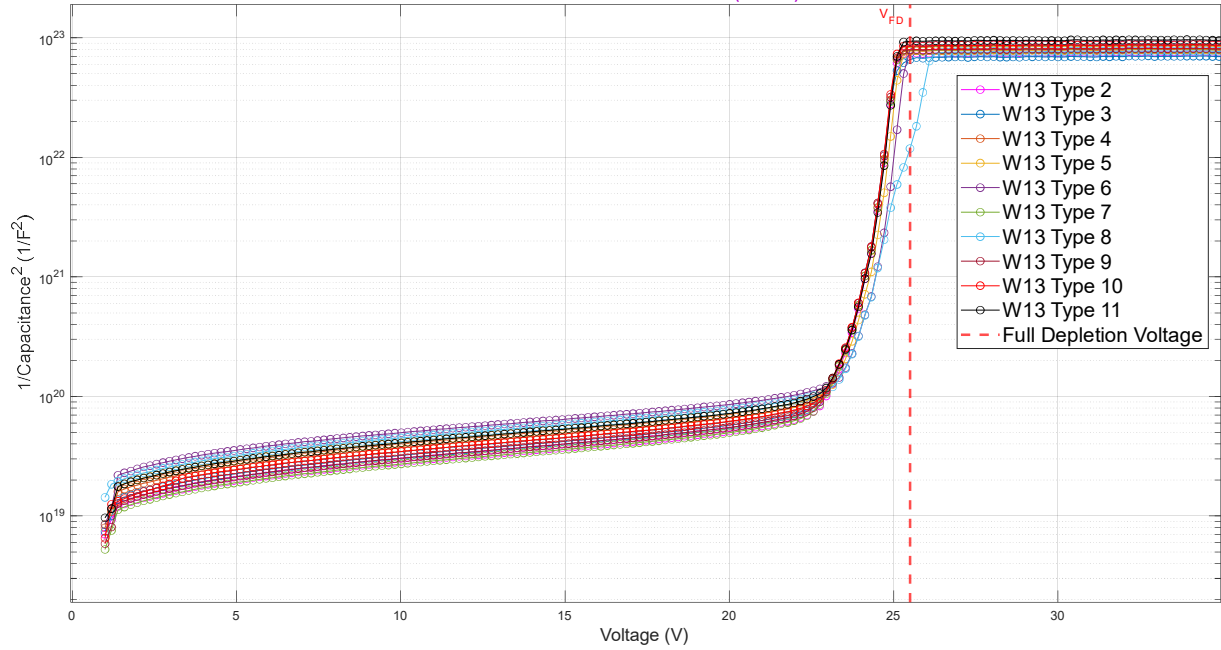


Figure 54. C-V characteristics for W13 sensors

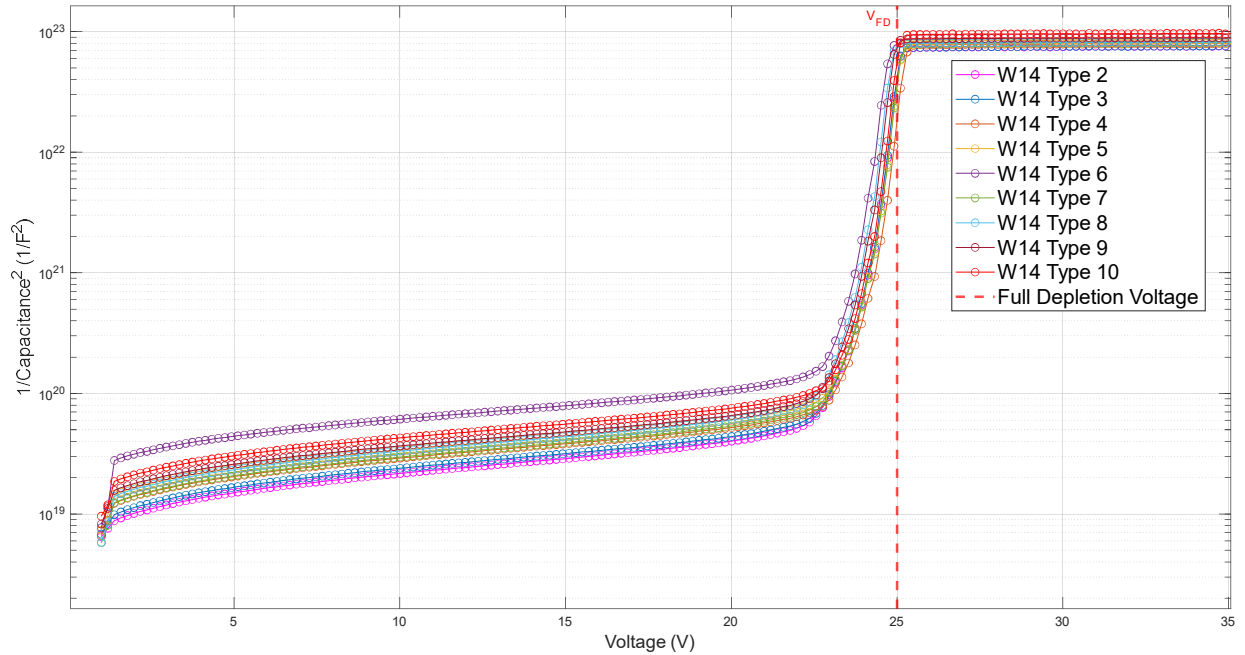


Figure 55. C-V characteristics for W14 sensors

The full depletion voltage is identified from  $1/C^2$  versus  $V$ , as shown in Figure 56. The curve corresponding to the under-depletion state (below  $V_{FD}$ ) of the detector is fitted

to a straight line of the constant nonzero slope, while the operation mode with the bias voltage higher than  $V_{FD}$  (over-depletion) is fitted by a straight line with almost zero slope. The intersection of the lines yields  $V_{FD}$ .

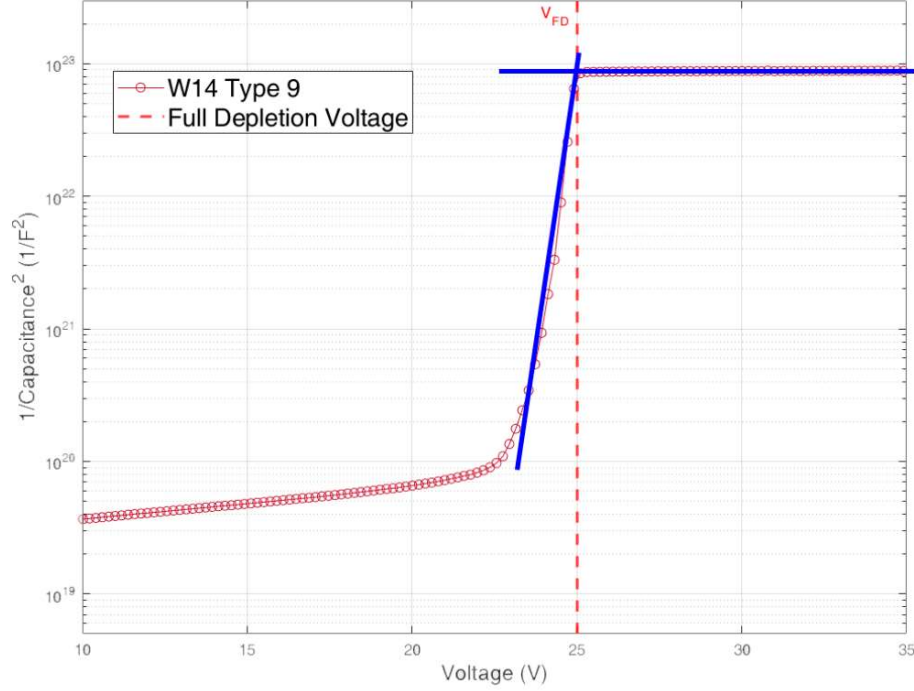


Figure 56. The C-V characteristic for the W14 Type 9 sensor; the full depletion voltage is determined as the intersection of the blue lines

Doping profiles are essential for the understanding of the performance of sensors and further simulations; however, manufacturers usually do not provide process details. One of the ways to obtain doping profiles is a C-V method - a non-destructive method which can be easily performed in a lab. To extract the data about the doping profile doped substrate assumed to be uniform and a semiconductor, a junction is considered to be sharp. The small thickness of the detector allows to apply the approximation for a parallel plate capacitor. Hence, if the depletion of the detector is not reached the depletion width  $x$  and the bias voltage  $V_b$  are connected with the doping concentration  $N$  by the expression [68]:

$$V_b = \frac{q \cdot N}{2\epsilon} x^2. \quad (39)$$

The measured capacitance  $C$  relates to the area  $A$  and the depletion width as [68]:

$$C = \varepsilon \frac{A}{x}. \quad (40)$$

The derivative of  $1/C^2$  with respect to  $V_b$  is proportional to  $1/N$  [68]:

$$N = \frac{2}{q\varepsilon A^2} \frac{1}{\frac{d}{dV} \frac{1}{C^2}}. \quad (41)$$

A capacitance-voltage characteristic of a detector can be transformed to an N-V scan and with the help of equation (40), eventually in an N-x graph. If the doping concentration is constant the  $\frac{1}{C^2}$  curve as a function of the bias voltage V is linear, what is reflected in equation (41). Doping profiles of W13 and W14 sensors are presented in Figures 57 and 58, respectively. The active area A of a pad was assumed to be  $1.3 \cdot 1.3 \text{ mm}^2$ .

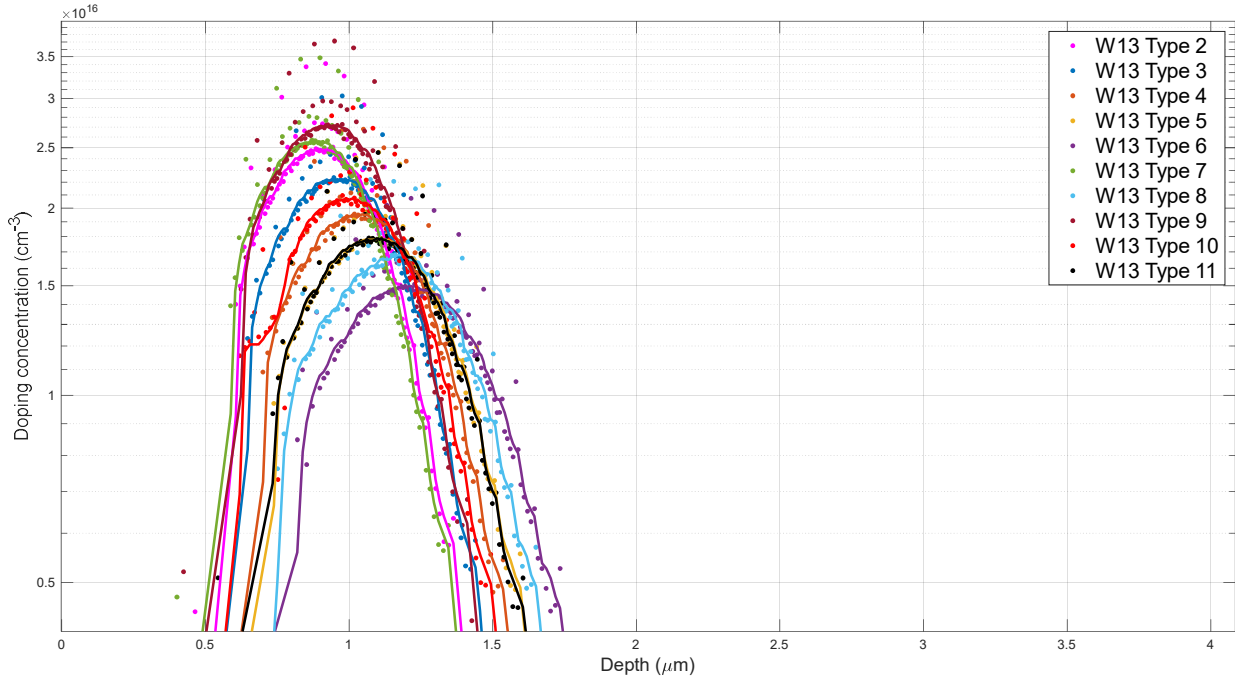


Figure 57. Doping profile obtained for W13 sensors

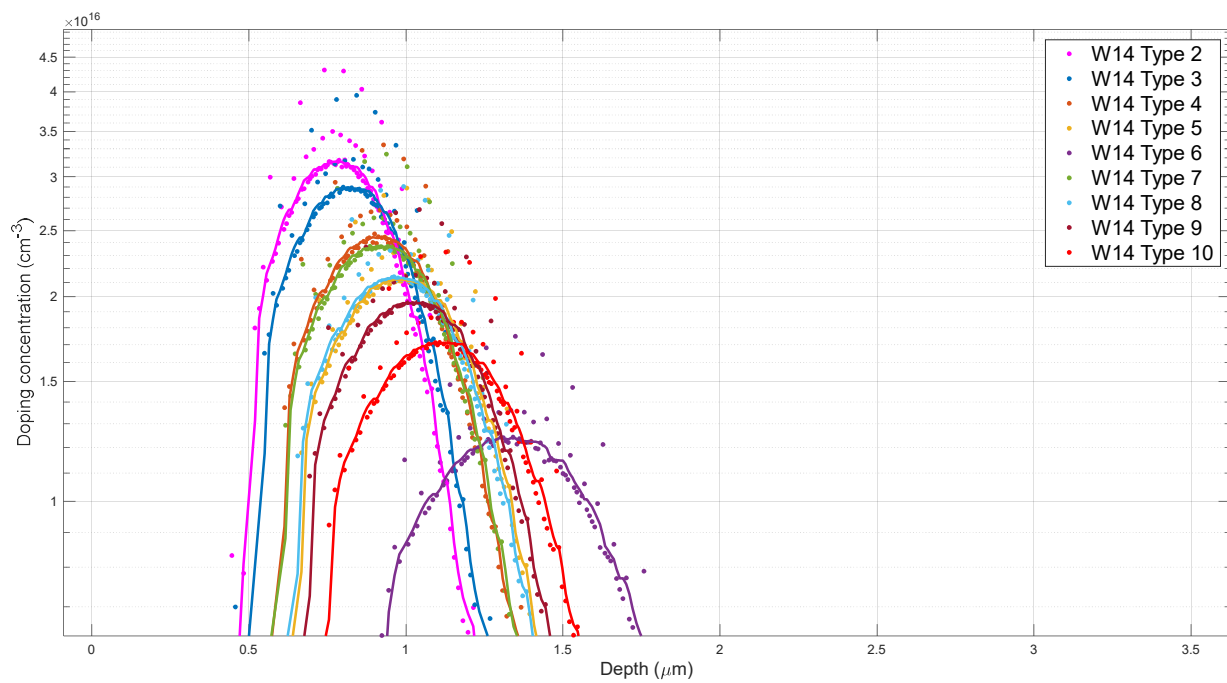


Figure 58. Doping profile obtained for W14 sensors

## 5.4 Discussion of the results

Considering the I-V characteristics shown in Figures 51 and 52, one can see a smooth increase of current with voltage, that at higher voltage leads to two completely different states. The first is a sudden abrupt increase in the current - an early breakdown. The second state is an exponential growth of the current value, which signifies an avalanche breakdown, typical for the Low Gain Avalanche Detectors.

Preliminary breakdown relates to phenomena inside the semiconductor sensor that occur due to small distances between areas with different doping concentration, and a large voltage gradient between electrodes. There are three potentially weak regions in the UFSD3.1 layout (Figure 59), where strong electric fields may develop:

1. The region where the corners of four pads meet: the four p-stops join here, creating a large p-doped structure
2. The region where the corners of two pads meet: two p-stops join here
3. The area along the p-stop between JTE and the guard ring.

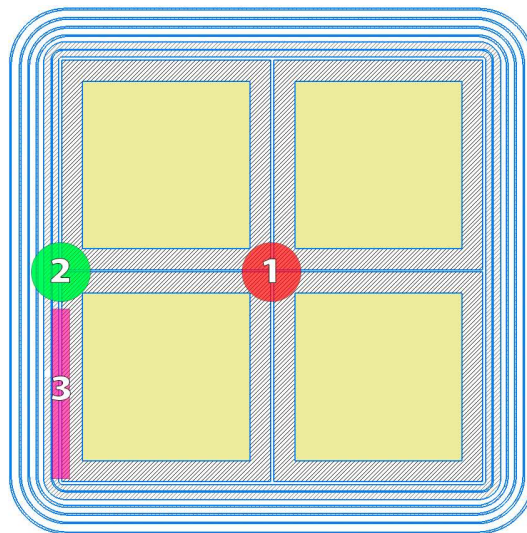


Figure 59. Sketch of the sensor with indicated areas where preliminary breakdown may occur

If the pads and the guard ring are set to 0 V while the p-stop has no connection, the latter experiences large tension, as it is only 50  $\mu\text{m}$  away from a very high negative bias below, and just few micrometers away from the pads at 0 V. Hence, the p-stops acquire a bias, which depends on many parameters, e.g. proximity of p-stop to the p-contact, the size of p-stop, the distance between p-stop and adjacent pads. Usually, this

bias is several volts; however, this voltage difference is enough to make the current flow resulting into early breakdown. Not only the small scale but also the doping of the p-stop influences breakdown voltage, as higher doping makes the p-stop more prone to acquire the bias from the p-contact. The last statement can be proven by comparing the results presented in Figures 51 and 52. All sensors belonging to the second group (W14) have a higher p-stop doping concentration with respect to the sensors of the first group (W13). Due to this reason, most of the sensors based on W14 and only a few of W13 sensors are suffering from an early breakdown. Hence, the first group of sensors could be excluded from further I-V analysis.

Radiation damage in silicon commonly leads to a decrease of the mean free path of the charge carriers, a reduction of the effective doping concentration, and the rise of the leakage current. In case of LGAD, one of the main effects is the deterioration of gain with fluence at a fixed voltage, that implies the need to increase the applied bias voltage after irradiation to at least partly compensate for this without electrical breakdown. Hence, the further the moment of breakdown is shifted towards the higher voltage, other things being equal, the longer the sensor lifetime in a hostile radiation environment is because in this case, the range of operating voltage values is wider. Almost all tested sensors satisfy the minimal requirement: the breakdown voltage of the unirradiated sensors should be at least 150 V, which is the voltage necessary for the free charge drift velocity saturation in 50  $\mu\text{m}$  silicon sensors. As can be seen from the graphs in Figures 51 and 52, for most of the W13 sensors, the upper limit of this range lies within 320-350 V. Moreover, all sensors from W13 wafer are measured to have a low leakage current level (sub-nA) at the *room temperature* before the breakdown, which is sufficient to keep the Shot noise low during the actual work of the device if the gain value is moderate.

During the measurements, the dependence of breakdown voltage as a function of the number of floating pads was investigated. In a real experiment, all pads of the sensor are bump bonded to the electronics (the read-out chip) and so fixed at 0 V. If the contact is missed, or if a channel of the electronics is malfunctioning, a floating pad appears.



The behaviour of the floating pad strongly depends on the way the sensor and p-stop are designed. By measuring the current with floating and grounded pads, one can estimate to what extent adjacent pads are isolated between each other. The aim of such measurements is to determine the optimal design and technological parameters, providing the widest range of the sensor operating voltage without preliminary breakdown.

Figures 51 and 52 show the I-V characteristics of sensors with none of the adjacent pads grounded by dashed lines. Dashed lines with round marks represent the situation when 2 adjacent pads are grounded. When adjacent pads are not set to 0 V the operating voltage decreases from 330 V to 300 V or in the worst case to 140 V. Considering the presented graphs, it can be seen that the Types 1, 2 and 11 have the lowest values of breakdown voltage while Types 4 and 10 - the highest.

Another crucial parameter of sensors connected with their future application in timing layers that should be considered when comparing the sensors is the fill factor; it corresponds to the portion of the detector which is able to detect particles efficiently. The narrower is a no-gain gap between adjacent pads the larger is the fill factor, thus the better is the particle detection efficiency. The design of Type 1 sensor has the “aggressive” strategy with the narrowest inter-pad gap within the production, 16  $\mu\text{m}$ , and Type 4 sensor is based on the “safe” strategy with the distance between adjacent pads of 24  $\mu\text{m}$ . It should be noted that Type 10 sensor built according to the “Super safe” strategy is the one which breakdown voltage is not affected by the lack of grounding; however, it has the largest inter-pad width of 49  $\mu\text{m}$  and hence the lowest fill factor.

From Table 2, one can see that the maximum values of the breakdown voltage in all grounding configurations, excluding Type 10 sensor are possessed by a Type 4 sensor. Therefore, in the first group of sensors, the Type 4 sensor has the optimal combination of large breakdown voltage and moderate inter-pad width.

The capacitance of the sensor strongly affects the timing performance of the whole time-measuring circuit. LGADs have C-V characteristics presented in Figures 54 and

55. The shape of C-V curve is determined by the inner structure of the sensor. The high capacitance at low bias voltages results from the incomplete depletion of the gain layer, and it is essential that multiplication layer is depleted for the gain. When the gain layer is depleted, the depletion region extends into the sensor bulk with less doping concentration than in the gain layer, and the value of capacitance significantly reduces, which is indicated as a “foot” in the C-V curve. All tested detectors are fully depleted at  $\sim 25\text{V}$ , which is beneficial in terms of lower power consumption, and capacitance of all sensors in full depletion mode is approximately  $3.5\text{ pF}$  while the requirements for the application of sensors in timing layers is  $4.3\text{ pF}$ .

Considering doping profile of tested sensors in Figures 57 and 58, the shift of the gain layer is observed, although the doping of the gain layer should be the same by design for all sensors within UFSD3.1 production. This fact can also be determined from C-V characteristics, as the “foot voltage” is proportional to the doping density of the gain layer, and it differs for all sensors. The origin of this shift is hard to establish. One possible reason could be incorrect interpreting of the C-V measurement due to parasitic capacitance of the measurement apparatus. In this case, C-V measurements could not be used for extracting the doping profile directly, and an additional correction factor is required. However, this has no impact on the detector performance once the sensor is fully depleted.

As a result of the measurements analysis, one can select the Type 4 sensor of interest to the further study and development with the following parameters: the concentration of the p-stop is  $1/20 \cdot F$ , the inter-pad gap is  $24\text{ }\mu\text{m}$ , the type of p-stop design is “grid”.

## SUMMARY

In this thesis, the study of Ultra-Fast Silicon Detectors was carried out. UFSDs are Low Gain Avalanche Detectors with a special gain layer tailored for timing measurements. During the latest research and development campaigns, UFSDs detectors have proven to accomplish the timing requirements of 30-35 picoseconds, satisfy constraints of limited thickness and radiation hardness for the timing layer for the next upgrade of the LHC. Nowadays, UFSDs are considered as suitable candidates to implement the 4D tracking as active elements of the HGTD and MTD, which are able to ensure accurate time and space measurements for a 4D reconstruction of the tracks. The CMS and ATLAS collaborations declared the addition of timing data as a potential solution that could help with the effects arising from the enhanced luminosity and which will allow the experiments to keep producing high-quality measurements.

The experimental study of the detectors was performed in the Detector Laboratory at the Helsinki Institute of Physics. During the experimental part two groups of 11 types 50  $\mu\text{m}$  thick UFSD3.1 manufactured by Fondazione Bruno Kessler (Italy) were tested. Sensors had different inter-pad widths, i.e. width between active areas of the sensor that multiply charge produced by the incident particle, guard structure (p-stop) designs and were based on two wafers W13 and W14 doped with two different concentrations of the acceptors in the p-stop.

To characterize the devices, two methods were employed: I-V measurements and C-V measurements. From I-V curves the breakdown voltage and the magnitude of leakage current were estimated, while C-V curves provided information about the depletion voltage, the capacitance of the sensors and the doping profile in the gain layer.

Almost all tested sensors had the breakdown voltage of at least 150 V, which is the voltage necessary for the free charge drift velocity saturation in 50  $\mu\text{m}$  unirradiated silicon sensors. However, most of the sensors based on W14 and only a few of W13 sensors were suffering from an early breakdown because sensors belonging to the second group (W14) had two times higher p-stop doping concentration than the sensors from the first group (W13).

During the measurements, the dependence of breakdown voltage as a function of the number of floating pads was investigated. By measuring the current with floating and grounded pads, it was estimated to what extent adjacent pads are isolated between each other. The aim of such measurements was to determine the optimal design and technological parameters, providing the widest range of the sensor operating voltage without preliminary breakdown.

Type 10 sensor is the one which breakdown voltage is not affected by the grounding of the adjacent pads; however, it had the largest among the tested detectors inter-pad width of 49  $\mu\text{m}$  and hence the lowest fill factor. The breakdown voltage of the Type 4 sensor was almost independent of the grounding; it is based on wafer W13 with an inter-pad gap 24  $\mu\text{m}$  and “grid” p-stop design. Therefore, the Type 4 sensor is of interest to further study and development.

The C-V curves were used to obtain doping profiles of tested sensors. Regarding the doping profiles, the shift of the gain layer is observed, although the doping of the gain layer should be the same by design for all sensors within UFSD3.1 production.

The future work should concentrate on the study of the origin of the doping profile shift. For this reason, a unified research methodology for all laboratories should be developed to avoid misinterpretations of the measurement results. Also, a large sample of I-V and C-V characteristics not only for W13 and W14 sensors but also for other sensors from the same batch should be assembled to complete the comprehensive picture of the sensors design parameters influence on the breakdown voltage. Another area of interest is a detailed study of UFSD3.1 parameter degradation with irradiation.

## REFERENCES

1. Article “Ten years on and the LHC accelerator is still not done colliding” [Online].  
- Available: <https://www.nikhef.nl/en/news/ten-years-on-and-the-lhc-accelerator-is-still-not-done-colliding/> (visited on 5.04.2020)
2. Nisati, A. Discovery of the Higgs Boson / A. Nisati. - San Diego, USA: UC San Diego, 2016.- P. 103-126
3. Aamodt, K. The ALICE experiment at the CERN LHC / K. Aamodt, [et all.] // Journal of Instrumentation.- 2008.- V. 3.- P. 260
4. Aad, G. The ATLAS Experiment at the CERN Large Hadron Collider / G. Aad, [et all.] // Journal of Instrumentation.- 2008.- V. 3.- P. 437
5. Chatrchyan, S. The CMS Experiment at the CERN LHC / S. Chatrchyan, [et all.] // Journal of Instrumentation.- 2008.- V. 3.- P. 361
6. Augusto Alves, A. The LHCb Detector at the LHC / A. Augusto Alves, [et all.] // Journal of Instrumentation.- 2008.- V. 3.- P. 217
7. Accelerator Performance and Statistics [Online].- Available: <http://acc-stats.web.cern.ch/acc-stats/#lhc/overview-panel>, (visited on 5.04.2020)
8. Frasciello, O. Wake Fields and Impedance Calculations of LHC Collimators' Real Structures / O. Frasciello // Editorial Series on Accelerator Science and Technology.- V. 38.- 2016.- P. 110-122
9. CMS Phase II Upgrade Scope Document [Online].- Available: <http://cds.cern.ch/record/2055167/files/LHCC-G-165.pdf?subformat=pdfa&version=4>, (visited on 10.04.2020)
10. ATLAS Phase-II Upgrade Scoping Document [Online].- Available: <http://cds.cern.ch/record/2055248/files/LHCC-G-166.pdf?version=2>, (visited on 10.04.2020)
11. Yohay, R. Precision timing for the high luminosity upgrade of CMS / R. Yohay // The 26th International Workshop on Vertex Detectors.- V. 28.- 2017.- P. 6-12.  
Available: <https://pos.sissa.it/309/028/pdf>
12. Faruqi, A.R. Electronic detectors for electron microscopy / A. R. Faruqi // Quarterly Reviews of Biophysics.- V. 44.- 2011.- P. 357-390

13. Lucchini, M. Development of the CMS MIP timing detector / M. Lucchini // Nuclear Instruments and Methods in Physics Research.- V. 958.- 2019.- P. 40-45
14. Siviero, F. Development of ultra-fast silicon detectors for 4D-tracking / F. Siviero // Incontri di Fisica delle Alte Energie - IFAE 2018.- V. 42.- 2019.- P. 194-200
15. Cartiglia, N. Timing layers, 4- and 5-dimension tracking / N. Cartiglia, [et all.] // Nuclear Instruments and Methods in Physics Research.- V. 924.- 2019.- P. 350-354
16. Technical Proposal for a MIP Timing Detector in the CMS Experiment Phase 2 Upgrade [Online].- Available: <http://cds.cern.ch/record/2296612/files/LHCC-P-009.pdf?version=5>, (visited on 12.04.2020)
17. Cartiglia, N. Tracking in 4 dimensions / N. Cartiglia, [et all.] // Nuclear Instruments and Methods in Physics Research.- V. 845.- 2017.- P. 47-51
18. Cartiglia, N. 4-Dimensional Tracking with Ultra-Fast Silicon Detectors / N. Cartiglia, [et all.] // Reports on Progress in Physics.- 2018.- V. 81.- P. 72-78.
19. Presentation “MIP Timing Detector for CMS Phase-II Upgrade” [Online].- Available:  
<https://indico.cern.ch/event/726024/attachments/1641419/2627172/mtdSeminarCERN-May4-2018.pdf> (visited on 12.04.2020)
20. Pellegrini, G. Technology developments and first measurements of Low Gain Avalanche Detectors (LGAD) for high energy physics applications / G. Pellegrini, [et all.] // Nuclear Instruments and Methods in Physics Research.- V. 765.- 2014.- P. 12-16. Available: <http://dx.doi.org/10.1016/j.nima.2014.06.008>
21. Cartiglia, N. Design optimization of ultra-fast silicon detectors / G. Pellegrini, [et all.] // Nuclear Instruments and Methods in Physics Research.- V. 796.- 2015.- P. 141-148. Available: <http://dx.doi.org/10.1016/j.nima.2015.04.025>
22. Kramberger, G. Radiation hardness of thin Low Gain Avalanche Detectors / G. Kramberger, [et all.] // Nuclear Instruments and Methods in Physics Research.- V. 891.- 2018.- P. 68-67
23. Ferrero, M. Radiation resistant LGAD design / M. Ferrero, [et all.] // Nuclear Instruments and Methods in Physics Research.- V. 919.- 2019.- P. 16-26. Available: <http://dx.doi.org/10.1016/j.nima.2018.11.121>

24. Corentin, A. A High-Granularity Timing Detector (HGTD) in ATLAS: Performance at the HL-LHC / A. Corentin, [et all.] // Nuclear Instruments and Methods in Physics Research.- V. 924.- 2019.- P. 355-359
25. Sze, S. M. Semiconductor Devices. Physics and Technology / S. M. Sze, M. K. Lee.- New York, USA: John Wiley & Sons, 2012.- P. 590
26. Lutz, G. Semiconductor Radiation Detectors / G. Lutz.- Berlin, Germany: Springer-Verlag Berlin Heidelberg, 2007.- P. 352
27. Bethe, H. On the stopping of fast particles and on the creation of positive electrons / H. Bethe // Proceedings of the Royal Society of London.- V. 146.- 1934.- P. 83-112
28. Hartmann, F. Evolution of Silicon Sensor Technology in Particle Physics / F. Hartmann.- Cham, Switzerland: Springer International Publishing AG, 2017.- P. 386
29. Ramo, S. Currents induced by electron motion / S. Ramo // Proceedings of the Institute of Radio Engineers.- V. 27.- 1939.- P. 584-585
30. Shockley, W. Currents to conductors induced by a moving point charge / W. Shockley // Journal of applied physics.- V. 9.- 1938.- P. 635-636
31. Presentation “Ultra-Fast Silicon Detectors” [Online].- Available: [http://physics.princeton.edu/~mcdonald/LHC/Cartiglia/Cartiglia\\_UFSD\\_TimingWG.pdf](http://physics.princeton.edu/~mcdonald/LHC/Cartiglia/Cartiglia_UFSD_TimingWG.pdf), (visited on 3.05.2020)
32. Parker, S. Increased speed: 3D Silicon Sensors; Fast Current Amplifiers. / S. Parker // IEEE Transactions on Nuclear Science.- V. 58.- 2011.- P. 404-416
33. Mota, M. A High-Resolution Time Interpolator Based on a Delay Locked Loop and an RC Delay Line / M. Mota, J. Christansen // IEEE Journal of Solid-State Circuits.- V. 34.- 1999.- P. 1360-1366
34. Jain, G. Dependence of charge multiplication on different design parameters of LGAD devices / G. Jain // Journal of Instrumentation.- V. 12.- 2017.- P. 150-155
35. Betta, G.-F.D. Design and TCAD simulation of double-sided pixelated low gain avalanche detectors / G.-F.D. Betta, [et all.] // Nuclear Instruments and Methods in Physics Research.- V. 796.- 2015.- P. 154-157. Available: <http://dx.doi.org/10.1016/j.nima.2015.03.039>

36. Van Overstraeten, V. Impact ionization in Silicon, a Review and Update / V. Van Overstraeten // Solid-State Electronics.- V. 33.- 1990.- P. 705-718
37. Scharf, C. Measurement of the drift velocities of electrons and holes in high-ohmic silicon / Scharf C., [et all.] // Nuclear Instruments and Methods in Physics Research.- V. 799.- 2015.- P. 81-89
38. Crowell, C. Temperature dependence of avalanche multiplication in semiconductors / C. Crowell // Applied Physics Letters.- V. 9.- 1966.- P. 242-244
39. Massey, D.. Temperature dependence of impact ionization in submicrometer silicon devices / D. Massey, [et all.] // IEEE Transactions on Electron Devices.- V. 53.- 2006.- P. 2328-2334
40. Moffat, N. Low Gain Avalanche Detectors (LGAD) for particle physics and synchrotron applications / N. Moffat, [et all.] // Journal of Instrumentation.- V. 13.- 2018.- P. 250-265
41. Presentation “Fast Timing and 4D Tracking with UFSD Detectors” [Online].- Available:  
<https://indico.cern.ch/event/710050/contributions/3161643/attachments/1739950/815149/AStaiano.pdf>, (visited on 23.04.2020)
42. Paternoster, G. Developments and first measurements of Ultra-Fast Silicon Detectors produced at FBK / G. Paternoster, [et all.] // Journal of Instrumentation.- V. 12.- 2017.- P. 170-175
43. Shimizu, Y. Impact of carbon co-implantation on boron distribution and activation in silicon studied by atom probe tomography and spreading resistance measurements / Y. Shimizu, [et all.] // Japanese Journal of Applied Physics.- V. 55.- 2016.- P. 250-260
44. Khan, A. Strategies for improving radiation tolerance of Si space solar cells / A. Khan, [et all.] // Solar Energy Materials and Solar Cells.- V. 75.- 2003.- P. 271-278
45. State-of-the-art and evolution of UFSD sensors design at FBK [Online].- Available:  
<https://indico.cern.ch/event/803258/contributions/3582777/attachments/1963858/265168/203-Arcidiacono-UFSDstatus.pdf>, (visited on 15.04.2020)



46. Baldassarri, B. Signal Formation in irradiated silicon detectors / B. Baldassarri, [et all.] // Nuclear Instruments and Methods in Physics Research.- V. 845.- 2017.- P. 20-23
47. Presentation “Measurements of Low Gain Avalanche Detectors (LGAD) for High Energy Physics applications” [Online].- Available: <https://indico.cern.ch/event/228876/>, (visited on: 20.04.2020)
48. Shockley, W. The Theory of p-n Junction in Semiconductors and p-n Junction Transistors / W. Shockley // The Bell System Technical Journal.- V. 28.- 1949.- P. 435
49. Herr, W. Concept of luminosity / W. Herr, [et all.] // CERN Accelerator School: Intermediate Course on Accelerator Physics, Zeuthen, Germany.- 2003.- P. 361-378. Available: <https://cds.cern.ch/record/941318/files/p361.pdf>
50. Presentation “HL-LHC Intro” [Online].- Available: [https://indico.cern.ch/event/607165/contributions/2581994/attachments/1463377/261187/4\\_-\\_HL-LHC\\_Introduction\\_Rossi.pdf](https://indico.cern.ch/event/607165/contributions/2581994/attachments/1463377/261187/4_-_HL-LHC_Introduction_Rossi.pdf), (visited on 8.05.2020)
51. Otero Ugobono, S. LGAD and 3D as Timing Detectors / S. Otero Ugobono // The 28th International Workshop on Vertex Detectors.- V. 373.- 2019.- P. 36
52. Fiorini, M. 4D fast tracking for experiments at the High Luminosity LHC / M. Fiorini, [et all.] // Proceedings of the 25th International Workshop on Vertex Detectors- V. 287.- 2017. Available: <https://pos.sissa.it/287/067/pdf>
53. A MIP Timing Detector for the CMS Phase-2 Upgrade [Online].- Available: <http://cds.cern.ch/record/2667167/files/CMS-TDR-020.pdf?version=2>, (visited on: 12.04.2020)
54. “Determination of 1 MeV Equivalent Neutron Fluence Using a P-I-N Dosimeter Diode” [Online].- Available: <https://www.osti.gov/etdeweb/servlets/purl/582543>, (visited on: 12.05.2020)
55. Presentation “From the pn-junction to the UFSD design” [Online].- Available: <http://personalpages.to.infn.it/~mandurri/teaching/MandurrinoSeminar29May2018.pdf>, (visited on 10.05.2020)

56. Article “How and why silicon sensors are becoming more and more intelligent?”  
[Online].- Available: <https://arxiv.org/ftp/arxiv/papers/1506/1506.05168.pdf>,  
(visited on: 20.04.2020)
57. Article “Passage of particles through matter” [Online].- Available:  
<http://pdg.lbl.gov/2005/reviews/passagerpp.pdf>, (visited on 15.04.2020)
58. Presentation “Particle interactions in particle detectors” [Online].- Available:  
[https://indico.cern.ch/event/294651/contributions/671929/attachments/552041/760669/Delmastro\\_ESIPAP2014\\_3.pdf](https://indico.cern.ch/event/294651/contributions/671929/attachments/552041/760669/Delmastro_ESIPAP2014_3.pdf) (visited on 5.05.2020)
59. X-ray imaging physics for nuclear medicine technologists. Part 1: Basic principles  
of X-ray production [Online].-  
Available: <http://tech.snmjournals.org/content/32/3/139/F4.expansion.html>, (visited  
on 20.04.2020)
60. Dragicevic, M. Qualification of a new supplier for silicon particle detectors. / M.  
Dragicevic, [et all.] // Nuclear Instruments and Methods in Physics Research.- V.  
732.- 2013.- P. 74-78
61. Presentation “Timing capabilities of Ultra-Fast Silicon Detector” [Online].-  
Available: <https://indico.cern.ch/event/273880/>, (visited on 30.04.2020)
62. Cantone, M.C. Radiation Physics for Nuclear Medicine. / M.C. Cantone, [et all.] /  
Springer, 2011.- P. 298
63. Presentation “Investigation of the Interstrip Isolation of p-type Strip Sensors”  
[Online].-  
Available: [https://indico.cern.ch/event/777112/contributions/3312261/attachments/1801061/2937768/Gosewisch\\_Isolation\\_of\\_p\\_type\\_sensors.pdf](https://indico.cern.ch/event/777112/contributions/3312261/attachments/1801061/2937768/Gosewisch_Isolation_of_p_type_sensors.pdf), (visited on  
5.05.2020)
64. Probe Systems Karl Suss PM8 [Online].- Available: <http://www.ptb-sales.com/manuals/karlsuss/pm8.pdf>, (visited on 5.06.2020)
65. Master’s Thesis “Prototype Evaluation of Silicon Sensors and Other Detector  
Components Suitable for Future CMS Tracker”, Shudhashil Bharthuar [Online].-  
Available: <https://helda.helsinki.fi/bitstream/handle/10138/299779/Shudhashil%20Bharthuar%20Final%20M.Sc%20.%20Thesis%20.pdf>, (visited on 5.06.2020)

66. Master's Thesis "Ultra-Fast Silicon Detectors and the Temperature Dependence of their response", Roberto Mulargia [Online]. - Available: <https://www.infn.it/>, (visited on 12.05.2020)
67. HiLumi in a nutshell [Online]. – Available: <https://project-hl-lhc-industry.web.cern.ch/content/hilumi-nutshell> (visited on 12.05.2020)
68. Galloway, Z. "Properties of HPK UFSD after neutron irradiation up to  $6 \times 10^{15}$  n/cm"/ Z. Galloway, [et al.] // Nuclear Instruments and Methods in Physics Research Section A: Accelerators, Spectrometers, Detectors and Associated Equipment. - 2019.